The Temporary Anions of Benzoxazole in Charge-Transfer Cluster Photodetachment

Beverly Feng, Sydney Cordova, Connor Fang, and Andrei Sanov *

Department of Chemistry and Biochemistry, University of Arizona, Tucson, Arizona 85721, United States

ABSTRACT. The photoelectron spectra of cluster anions of superoxide (O_2^-) solvated by one molecule of benzoxazole (BzOx) reveal two competing photodetachment mechanisms: a direct photoemission from the solvated cluster core and an indirect pathway involving temporary anion states of benzoxazole accessed via the O_2^-·BzOx → O_2·$BzOx^-$ charge-transfer transitions. Benzoxazole is a bicyclic unsaturated organic molecule that does not form permanent anions. However, its low-lying vacant π* orbitals permit a resonant capture of the electron emitted from the O_2^- cluster core. The non-Hermitian theory using a complex absorbing potential predicts the existence of two $BzOx^-$ π* resonances within the experimental energy range: resonance A (π_1^*) at 0.891 eV and resonance B (π_2^*) at 1.76 eV, relative to the onset of the BzOx + e^- continuum at the ground-state geometry of neutral BzOx. Within the clusters, the O_2·$BzOx^-$ charge-transfer states are partially stabilized relative to the free-electron limit by interactions with the O_2 molecule. These interactions depend on the electronic states of both species. The theory predicts that at the O_2^-·BzOx cluster geometry, the $O_2(X^3\Sigma_g^-)$·$BzOx^-$(A) and $O_2(a^1\Delta_g)$·$BzOx^-$(A) states lie at 0.56 eV and 0.47 eV (vertically) above the respective neutral states. The $O_2(^3\Sigma_g^-)$·$BzOx^-$(B) resonance is found 1.43 eV (vertically) above $O_2(X^3\Sigma_g^-)$·BzOx. Intense signatures of both $BzOx^-$ resonances and the three abovementioned charge-transfer cluster states, $O_2(X^3\Sigma_g^-)$·$BzOx^-$(A), $O_2(a^1\Delta_g)$·$BzOx^-$(A), and $O_2(^3\Sigma_g^-)$·$BzOx^-$(B) are observed in the 355 nm (3.495 eV) and 532 nm (2.330 eV) photoelectron spectra of the O_2^-·BzOx cluster anion.

1. Introduction

From astrophysics to biochemistry, temporary anions play important roles in many branches of scientific inquiry.[1-5] The reason is rooted in the reactivity of these species. Despite—or rather because of—their transient nature, anionic resonances embedded in the free-electron continuum may turn the host molecules into large scattering targets and short-lived reactive intermediates.

Signatures of temporary-anion resonances are observed in electron scattering on atoms and molecules,[6-11] as well as in the photoelectron spectra and other observables associated with molecular and cluster anions.[12-20] Clusters in particular have long been viewed as unique microscopic laboratories for observing intermolecular reactivity in the (sub-)nanoscale regime,[21-28] presenting rich opportunities for the studies of resonances.

Electron photodetachment from a negatively charged cluster is generally expected to yield recognizable spectral signatures of the core anion, with the bands shifted and broadened by the interactions among the cluster constituents.[24] However, this expectation discounts the interactions of the departing electron with the solvent molecules, regarding them as mere spectators of the photodetachment transition occurring within the solvation-stabilized cluster core. This view is justified only if the electron-solvent scattering is small. In the presence of solvent-based anionic resonances, the electron-solvent interactions may play a prominent role, including the formation of short-lived charge-transfer states.[6-7,9,29]

These states may turn cluster photodetachment into an indirect process, and all observables must be analyzed accordingly. At a minimum, a temporary capture of the electron by a solvent-based resonance is likely to scramble its phase and angular momentum, resulting in a well-documented loss of anisotropy in the photoelectron angular ditributions.[12,30-31] In the energy domain, the photoelectron spectra may show a cross-section enhancement in the vicinity of the resonance.[32]

All in all, the experimental observables will reflect not only the properties of the solvated cluster core but also the electronic structure and dynamics of the solvent-based transient anions.

There are many examples of solvent-based anionic resonances in cluster anion photodetachment.[12,30-35] In relation to the present work, we highlight the recent investigations by Jarrold and coworkers,[32,34-35] who examined the temporary anion states associated with the unsaturated π systems of benzene and its substituents. In O_2^-·benzene cluster photodetachment at 355 nm (3.495 eV), they observed a significant enhancement of the $O_2^- \rightarrow O_2(a\,^1\Delta_g)$ transition within the core anion, relative to the lowest-energy $O_2^- \rightarrow O_2(X\,^3\Sigma_g^-)$ photodetachment band.[32] The enhanced transition was observed at electron kinetic energies of 0.5-1.5 eV and its amplification was attributed to a benzene anionic resonance[7,36] within this range.

In the present work, we consider benzoxazole (BzOx), a bicyclic unsaturated molecule with a molecular formula C_7H_5NO. It consists of a five-membered heterocyclic ring of 1,3-oxazole fused with a benzene ring at oxazole's 4,5-positions, as can be discerned in the O_2^-·BzOx cluster structures shown in Figure 1. As a keystone reactant for the synthesis of biologically active molecules in medicinal chemistry,[37-41] its reactivity is of not only fundamental but also practical importance. Similar to benzene,[32] BzOx on its own does not form permanent anions, but this does not mean that it is unreactive towards electrons. Like many other organic molecules,[11] BzOx possesses several vacant π* orbitals capable of accepting low-energy electrons in temporary-anion states.

We access these states via the O_2^-·BzOx cluster photodetachment, in a manner similar to Jarrold and coworkers' O_2^-·benzene experiment.[32] The oxygen molecule has a positive electron affinity of 0.448(6) eV,[42] contrasting the nonexistent (i.e., negative) affinity of BzOx, so the initial charge placement within the cluster is not in question. In the photodetachment, two photoemission mechanisms can be envisaged. The first is a direct process involving a solvation-stabilized O_2^-

cluster core. The second is an indirect pathway in which a resonance associated with charge transfer from O_2^- to benzoxazole leads to the formation of a temporary $BzOx^-$ anion.

To discriminate between these mechanisms, we compare the O_2^-·BzOx results to similar measurements on O_2^-·H_2O.[43-48] Unlike BzOx, water molecules do not possess anionic resonances in the experimental energy range.[36] In fact, comparisons to water were previously used to reveal the role of resonances in the photodetachment of I^-·CH_3I,[30] $(aceton)_n^-$,[33] $NO^-(N_2O)_n$,[12,31] and $O^-(N_2O)_n$,[31] clusters, just to name a few.

The key molecular orbitals (MOs) involved in this study are shown in Figure 1. Rigorous theory will be presented later in Section 4; here, to set the stage, we discuss a qualitative picture based on density-functional calculations. Parts (a) and (b) on the left side of Figure 1 represent a restricted canonical view. The doubly degenerate π* MOs of O_2^- are shown in (a). In the ground $^3\Sigma_g^-$ state of neutral O_2, both are singly occupied with same-spin electrons. In O_2^- ($^2\Pi_g$ ground state), one is doubly occupied, while the other contains one electron. In the presence of a solvent molecule, the degeneracy between the two canonical HOMOs is lifted, as illustrated in Figure 1(b). Similar to O_2^-·benzene,[32] the ground state of O_2^-·BzOx is of a $^2A''$ electronic symmetry. That is, in the O_2^-·BzOx cluster, the A′ (in-plane) π* MO of O_2^- (π′ for short) is doubly occupied, while its A″ (out-of-plane) counterpart (π″) is singly occupied. This corresponds to a $\ldots(\pi')^2(\pi'')^1$ electron configuration, which places the greatest O_2^- electron density in the BzOx molecular plane, thus maximizing the solvation interactions within the cluster.

The above simplified—restricted—picture may lead to incorrect conclusions if taken too far. For example, Figure 1(b) seems to suggest that the lowest-energy photodetachment transition in O_2^-·BzOx would proceed via electron removal from the singly occupied π″ HOMO of the cluster. Such a transition would yield the $^1\Delta_g$ state of O_2, which is not the lowest neutral state. Shown on

the right side of Figure 1 in part (c) is an unrestricted picture of the cluster MOs. The occupied α-spin version of the π″ orbital is in fact lower in energy than its π′ counterpart, while the vacant β-spin π″ MO is much higher. The lowest-energy photodetachment from O_2^-·BzOx corresponds to electron removal from the β-space π′ MO, which is in turn associated with the $O_2^- \rightarrow O_2(X^3\Sigma_g^-)$ transition within the cluster core.

Also included in Figure 1(c) is the π* LUMO of BzOx. The O_2^-·BzOx → O_2·$BzOx^-$ charge-transfer transitions considered in this work are described approximately as electron transfer from the O_2^- MOs in the occupied part of Figure 1(c) to the α- or β-π* LUMO of BzOx. However, electron detachment/attachment transitions are inherently many-body processes, which cannot be adequately described in terms of single canonical orbitals.[49-52] This brings us to what truly enables the interpretation of temporary-anion experiments in the modern age: the availability of highly accurate yet efficient computational methods[49,53-54] to describe metastable states and photodetachment transitions for direct quantitative comparison with the experiment.

In what follows, we use photoelectron imaging spectroscopy to investigate the O_2^-·BzOx clusters in comparison to O_2^-·H_2O. We demonstrate that whereas the direct photodetachment mechanism adequately describes the latter, it does not yield quantitative agreement with the O_2^-·BzOx data. We follow up these results with a theory investigation of the low-lying temporary anion states of benzoxazole. The non-Hermitian theory reveals the existence of not one but two $BzOx^-$ resonances contributing to our experimental measurements. We then show that only by including these temporary charge-transfer states and their interactions with the neutral O_2 molecule is it possible to accurately model and interpret the O_2^-·BzOx photoelectron spectra.

2. Experimental and Theoretical Methods

The experimental apparatus has been described elsewhere.[55-57] Oxygen gas at a pressure of 1.4 atm was passed through a sample holder containing a small amount of benzoxazole. The sample holder was kept at a temperature close to benzoxazole's melting point of 31°C. The resulting mixture of BzOx (vapor pressure 0.25 torr at room temperature) and O_2 was expanded into the ion source chamber through a pulsed (50 Hz) supersonic nozzle (General Valve Inc., Series 9). The source chamber is maintained at a base pressure of 2×10^{-7} torr, which increases to $2\text{-}3\times10^{-5}$ torr when the nozzle is operating.

Electrons were emitted from a thoria-coated iridium filament (e-Filaments, LLC) floated at a negative potential of ~100 V and heated by a direct current of ~5 A. The tip of the filament was positioned close to the nozzle axis, but many nozzle diameters downstream from the orifice.[58] This arrangement has been previously described as the "electron cannon"[59] (in contrast to the customary "electron gun"[21]) and has been shown to result in ion temperatures of ~700 K.[58,60] Approximately 30 cm downstream from the nozzle, a 40 cm diameter metal plate was rapidly (10-15 ns) pulsed down to −700 to −900 V sending the negative ions from the supersonic plasma into the ~2 m long flight tube of a Wiley-McLaren[61] time-of-flight mass spectrometer.[55]

A representative mass spectrum of the anions formed under these conditions is shown in Figure 2. Most peaks correspond to the hydrated superoxide series, $O_{2n}^-(H_2O)_m$.[43-45,48,62-76] Their plausible assignments are indicated in the figure in black. Four peaks labeled in red are attributed to ions containing benzoxazole or its derivatives. The 76 a.m.u. peak is assigned to the *o*-benzyne radical anion, $C_6H_4^-$.[77-80] We hypothesize that it may form via the fission of the benzene and oxazole rings upon electron capture by benzoxazole, likely via a σ* $BzOx^-$ resonance (possibly coupled to one of the π* resonances studied in this work). The 118 a.m.u. peak is assigned to deprotonated

benzoxazole, i.e., the benzoxazolide anion. Its photoelectron spectra will be reported in an upcoming publication. The next peak labeled in red is identified as O_2^-·BzOx (151 a.m.u.), i.e., the superoxide anion solvated by a benzoxazole molecule. It is the object of this work. Finally, the peak at 183 a.m.u. is similarly assigned to the O_4^-·BzOx cluster, which is not studied here.

The mass-selected O_2^-·BzOx ions were irradiated by a collimated 532 or 355 nm laser beam. The 7 ns pulses were produced as a second or third harmonic, respectively, of a Spectra Physics Lab-130-50 Nd:YAG laser operated at 50 Hz, matching the repetition rate of the ion source. The photoelectrons were projected on a position-sensitive detector using a velocity-map[81] imaging[82-83] lens.[56] The photoelectron images were analyzed following published procedures[57,84] using the BASEX program developed by Reisler and co-workers[85] for the inverse Abel transformation.[83]

The Franck-Condon simulations[86-88] of the isolated and solvated O_2^- photoelectron spectra were carried out using a custom program which assumed Morse potentials for the electronic states of O_2^- and O_2. Using the spectroscopic parameters determined by Lineberger and coworkers,[42] the program computed the Morse-oscillator wavefunctions[89] for various vibrational levels of each electronic state. These were used for direct computation of the overlap integrals (the Franck-Condon factors). The resulting stick spectra were scaled by a Wigner-like[90-91] power-function to account for the electronic cross-section's eKE dependence[58,92-96] and convoluted with a Gaussian broadening function matching the conditions of each experimental measurement.

A non-Hermitian framework using the complex absorbing potential (CAP) method[97] was used to characterize the O_2·$BzOx^-$ charge-transfer states. The CAP methodology was combined with the equation-of-motion (EOM) electron-attachment (EA) coupled-cluster (single and double excitations, i.e., CCSD) methods.[53,97-98] All calculations were performed using the Q-Chem 5.1 program package[99] licensed to our research group. Additional details are provided in Section 4.

3. Experimental Results and Initial Analysis

The raw and Abel-inverted photoelectron images of O_2^-·BzOx obtained with 355 nm (3.495 eV) and 532 nm (2.330 eV) light are shown in Figure 3(a) and (b). The light polarization is vertical in the image plane, but the observed transitions are mostly isotropic.

The photoelectron spectra obtained from the images are presented in Figure 3(c) and (d) in black. All spectra are plotted with respect to electron kinetic energy (eKE), shown at the top axes, and electron binding energy, eBE = $h\nu$ – eKE, shown along the bottom axes. In both panels, the O_2^-·BzOx results are compared to the corresponding O_2^-·H_2O spectra (light blue). The O_2^-·H_2O photoelectron images (not shown) were obtained on the same instrument under conditions similar to the O_2^-·BzOx results. The O_2^-·H_2O spectra are similar to the data for this system previously reported by our group[47-48] and others.[43-45]

3.1. The O_2^- spectra. We begin the analysis by considering the well-characterized photoelectron spectrum of O_2^-.[32,34-35,42,100-102] Figures 3(c) and (d) include the Franck-Condon simulations of the O_2^- spectra at respective wavelengths, shown by green dotted lines. The simulated spectra bear very close resemblance to the experimental data obtained under similar conditions by our group and others.[32,34-35,42,47-48,102] The model, rather than experimental O_2^- spectra, are shown here with the next step in mind: modeling of the cluster data.

The 355 nm O_2^- spectrum in Figure 3(c) consists of three vibrationally-resolved bands corresponding to O_2^- photodetachment to the $X^3\Sigma_g^-$, $a\ ^1\Delta_g$, and $b\ ^1\Sigma_g^+$ electronic states of neutral O_2.[42,103] In Figure 3(d), the 532 nm $a\ ^1\Delta_g$, and $b\ ^1\Sigma_g^+$ band intensities are noticeably suppressed relative to the $X^3\Sigma_g^-$ band. This is due to the centrifugal barrier inhibiting the cross-section for low-eKE electrons. In photodetachment from the d-like π* HOMO of O_2^-, the electric dipole allowed partial waves have the lowest l value of 1, corresponding to a Wigner exponent of 3/2.[90-91]

3.2. Direct photodetachment of solvated O_2^-: the case of $O_2^-\cdot H_2O$. Next, we consider the $O_2^-\cdot H_2O$ data in Figure 3(c) and (d). This cluster too has been studied extensively, and the interpretation of its photoelectron spectrum is well-established.[43-48] By comparing the 355 nm O_2^- and $O_2^-\cdot H_2O$ spectra in Figure 3(c), the following observations are made. While the overall envelope of the O_2^- spectrum is retained as a signature of $O_2^-\cdot H_2O$, the cluster bands are shifted by the amount of solvation energy, and the transitions become so congested due to the additional degrees of freedom in the cluster that all vibrational band structure is lost. As a result, the 355 nm $O_2^-\cdot H_2O$ spectrum consists of two congested, nearly overlapping bands attributed to core-anion photodetachment to the $X\,^3\Sigma_g^-$ and $a\,^1\Delta_g$ states of O_2. The $b\,^1\Sigma_g^+$ band is not observed: its solvation-stabilized binding energy exceeds the photon energy. For similar reasons, the 532 nm $O_2^-\cdot H_2O$ spectrum in Figure 3(d) consists of a single congested band attributed to core-anion photodetachment to the $X\,^3\Sigma_g^-$ state of O_2.

Figures 4(a) and (b) compare the experimental $O_2^-\cdot H_2O$ spectra (blue) with the Franck-Condon simulations (red) based on the broadened and shifted O_2^- spectra. Details are in Supporting Information (SI), but the key assumptions include significant band broadening and a solvation energy of $\Delta E_{solv} = 1.33$ eV. These and other assumptions were applied consistently to the 355 and 532 nm data. In sum, the $O_2^-\cdot H_2O$ experimental spectra are readily understood in terms of direct photodetachment from the core O_2^- anion stabilized by solvation. For extra clarity, Figures 4(a) and (b) include the Franck-Condon simulations of the O_2^- spectra shifted by the above ΔE_{solv}. The $O_2^-\cdot H_2O$ spectra have similar envelopes, subject to additional broadening.

3.3. $O_2^-\cdot$BzOx is different. Now we turn to the $O_2^-\cdot$BzOx spectra in Figure 3(c) and (d). At a first glance, one might be inclined to interpret these data similar to $O_2^-\cdot H_2O$, in terms of the O_2^-

bands shifted and broadened by interactions with the BzOx solvent molecule. The two broad bands in the 355 nm O_2^-·BzOx spectrum in Figure 3(c) would then be attributed to the $X^2\Pi_g \rightarrow X^3\Sigma_g^-$, $a\,^1\Delta_g$ direct photodetachment transitions within the cluster core, like in the O_2^-·H_2O case, but with a smaller solvation-induced shift due to BzOx.

Upon closer inspection, this interpretation is inconsistent with the results. First, the spacing between the two bands in the 355 nm spectrum of O_2^-·BzOx is larger than that between the $X^3\Sigma_g^-$ and $a\,^1\Delta_g$ bands in the O_2^-·H_2O spectrum. Second, the lower-eBE band in O_2^-·BzOx is significantly broader than the $X^3\Sigma_g^-$ band in O_2^-·H_2O. Because of the first point and despite the second, the two O_2^-·BzOx bands are better separated from each other than the two O_2^-·H_2O bands. Third, the second (higher-eBE) band in the O_2^-·BzOx spectrum is significantly enhanced relative to the first, despite the expected Wigner suppression.[90-91]

To elaborate on these differences, Figure 4(c) shows two attempts to model the 355 nm O_2^-·BzOx spectrum using the same basic assumptions that had worked for O_2^-·H_2O in Figure 4(a). In (c), a shifted O_2^- spectrum can match either the maximum of the first O_2^-·BzOx band or its low-eBE onset, but not both. The dark-blue and red simulations in Figure 4(c) illustrate these different scenarios. They assume the same simulation parameters as those used for the O_2^-·H_2O spectrum in Figure 4(a), but with different solvation energies: ΔE_{solv} = 0.80 eV (red) or 1.02 eV (blue). The green trace in (c) represents the O_2^- spectrum shifted by 0.80 eV. Between the red and blue model spectra, red is a better match to the observed spectral onset, and the corresponding solvation energy is closer to the ab initio values. We will use ΔE_{solv} = 0.80 eV in most subsequent modeling.

Neither the red nor the blue direct-detachment simulations provide satisfactory matches to the overall 355 nm O_2^-·BzOx spectrum in Figure 4(c). The same assumptions are entirely inconsistent with the 532 nm spectrum. In Figure 4(d), the red and blue model traces use the same assumptions

as their counterparts in Figure 4(c), just for a different wavelength. Neither simulation matches the experimental band.

3.4. The missing physics. In sum, it is impossible to model the 355 and 532 nm spectra of O_2^-·BzOx in terms of direct photodetachment from a solvated cluster core. The direct model ('red' or 'blue') cannot account for the eBE ≈ 3.0 eV (eKE ≈ 0.5 eV) spectral region in Figure 4(c). The favored 'red' model also misses some signal near eBE ≈ 2.0 eV (eKE ≈ 1.5 eV). A similar conclusion pertains to the 532 nm spectrum in Figure 4(d).

Therefore, some essential physics is missing in the direct-photodetachment model for O_2^-·BzOx. The key to the puzzle is suggested by Jarrold and coworkers, who studied the photodetachment of O_2^- solvated by various volatile organics.[32,34,104-105] They observed a spectral enhancement in the $a\,^1\Delta_g$ transition region (eKE ≈ 1.0 eV at 355 nm) in O_2^- solvated by benzene and attributed it to a solvent-based anionic resonance.[32,34] The comparison of the O_2^-·BzOx and O_2^-·H_2O spectra leads us to a similar conclusion: that an anionic resonance associated with benzoxazole's unsaturated π system may be responsible for the observed differences. To investigate this hypothesis, we turn to the theory of anionic resonances in the benzoxazole molecule.

4. Theory Results

The temporary anion states of isolated benzoxazole and the O_2·$BzOx^-$ charge-transfer cluster states were investigated using non-Hermitian CAP-EOM-EA-CCSD methodology.[53,97-98] Most work was done for the optimized geometry of BzOx, but several calculations in Section 4.5 were carried out for the O_2^-·BzOx cluster structure. The ground-state geometries of the BzOx molecule and O_2^-·BzOx cluster were optimized at the CCSD level with the aug-cc-pVDZ basis set.

4.1. Diffuse basis functions. The nature of temporary anion states necessitates the use of very

diffuse bases. All CAP calculations used the aug-cc-pVDZ basis set augmented with three sets of additional p and d diffuse functions, 3p3d. Since there are three different p and five d functions in each set, 9 p and 15 d functions were added in total. The added p and d functions were placed at benzoxazole's (not the cluster's) center of nuclear charge. The resulting basis set is referred to as aug-cc-pVDZ+3p3d(C),[97] where C stands for 'center'. No extra s functions were included because they do not contribute to the target π states of A″ symmetry.

The exponent of the first added function of each type was 1/2 of the most diffuse carbon exponent of that type in the aug-cc-pVDZ basis. All subsequent exponents were scaled progressively by 1/2.[97,106-107] For illustration, the least and most diffuse added p_z and d_{xz} functions are shown in Figure 5.

4.2. CAP-free Dyson orbitals. Electron attachment to a molecule affects the electrons already present in it. This inherently many-body process is appropriately described using Dyson rather than canonical (Hartree-Fock or Kohn-Sham) orbitals.[49-52] In electron attachment to benzoxazole, the Dyson orbitals are defined by the overlap integrals between the 63-electron wave function of $BzOx^-$ and the 62-electron neutral BzOx state.

We begin by considering the CAP-free EOM-EA-CCSD calculations for the $BzOx^-$ anion. They were performed at the optimized geometry of benzoxazole, using its ground-state $^1A'$ wave function as a reference. Figure 6 summarizes seven lowest-energy EA solutions of A″ symmetry. All attachment energies at the top of the figure are real (because these solutions are CAP-free) and positive (because the $BzOx^-$ states are unbound).

The corresponding Dyson orbitals have intricate structures. To simplify their examination, each orbital in Figure 6 is shown using three different isosurface (iso) values, orientations, and zoom levels. The iso values used are 0.003, 0.008, and 0.016 a.u. (top to bottom). The smallest

value brings out the diffuse pseudocontinuum parts of the orbitals, while the largest—the valence parts. The different-iso plots are each shown for a different orientation of the molecular frame. In the top row (iso = 0.003), the BxOx plane (*xy*) is perpendicular to the page, corresponding to the same orientation as in Figure 5. In the middle and bottom rows (iso = 0.008 and 0.016), the molecule is tilted about the *x* axis by 30° and 60° degrees, respectively, to permit clear views of the valence π system. The plots in the middle and bottom rows are magnified ×1.5 and ×2, respectively, compared to the top. Similar display schemes are used in several subsequent figures.

Root 1 in Figure 6 represents the smallest attachment energy and the most diffuse Dyson orbital. Its properties are dictated by the incomplete basis, and its energy is determined by the most diffuse basis functions. To illustrate this point, the expanded aug-cc-pVDZ+4p4d(C) basis set with an extra set of diffuse functions results in a more diffuse Dyson orbital for root 1, lowering its energy from 0.267 eV to 0.133 eV. In a complete-basis limit, this solution would turn into a free electron with an attachment energy of asymptotically zero.[54]

While root 1 as well as roots 4, 5, and 7 in Figure 6 are diffuse, predominantly pseudocontinuum states, roots 2, 3, and 6 in contrast exhibit significant contributions from the BzOx π MO system. The iso = 0.016 plots of roots 2 and 3 both have the distinct characteristics of the canonical LUMO (π_1^*) from Figure 1. However, the diffuse parts of these orbitals (top and middle rows in Figure 6) are different, indicating that these two states result from couplings of the same BzOx LUMO with different pseudocontinuum states. Dyson orbital #6 possesses the features of a higher-energy canonical π* orbital of BzOx (π_2^*).

4.3. Complex absorbing potential and non-Hermitian solutions. Transient states, by definition, do not correspond to single molecular eigenstates in Hermitian quantum mechanics.[108-109] Therefore, none of the CAP-free solutions in Figure 6 represent temporary $BzOx^-$ anions. None-

theless, the anion properties can be determined by means of artificial stabilization[110] of some of the above solutions. This can be achieved by augmenting the Hamiltonian with a CAP term:

$$H(\eta) = H_0 - i\eta W \quad (1)$$

where H_0 is the (Hermitian) molecular Hamiltonian, and W is an artificial absorbing potential scaled by a strength parameter η. For reviews of the theoretical foundation and practical implementation of this approach, the reader is referred to the seminal papers by Krylov and coworkers,[53-54,97] as well as the references cited therein.

In our calculations, we assumed a parabolic W function in Eq. 1 with a cuboid onset boundary represented by a $2x_0 \times 2y_0 \times 2z_0$ box. The box dimensions were defined by the spatial extent of the X^1A' reference wave function of neutral BzOx: $x_0 = \langle X^2 \rangle^{1/2}$ = 25.1 bohr, $y_0 = \langle Y^2 \rangle^{1/2}$ = 17.3 bohr, and $z_0 = \langle Z^2 \rangle^{1/2}$ = 6.4 bohr. Two different projections of this box are shown in Figure 7 along with one of the CAP-free Dyson orbitals from Figure 6 (root #3, iso = 0.003).

While the CAP-free solutions in Figure 6 correspond to η = 0 (Eq. 1), we carried out many CAP-EOM-EA-CCSD/aug-cc-pVDZ+3p3d(C) calculations using various values of η > 0. Each calculation required >1 day of CPU time (which is why this work is limited to the modest double-ζ valence basis). The non-Hermitian solutions are represented by complex energies and complex Dyson orbitals. The energy eigenvalues depend on η and can be expressed as $E(\eta) = E_R(\eta) - i\Gamma(\eta)/2$, where E_R = Re(E) and Γ = –2Im(E) are the resonance position and width.[53,97-98]

The CAP has varying effects on the different EOM-EA-CCSD solutions. With η > 0, many of the CAP-free roots in Figure 6 transform into roots with large negative magnitudes of Im(E). This is particularly true of the states with large diffuse contributions (roots 1, 4, 5, and 7). Rather than being stabilized, these pseudocontinuum states are absorbed by the CAP and present little interest to our investigation. But two solutions, those arising from roots 3 and 6 (Figure 6), exhibit stabil-

ized signatures. We will be referring to them as resonances A and B, respectively. Using the scattering nomenclature, they can be described alternatively as π_1^* and π_2^*, but these labels should not be confused with the π^* (π' and π'') MOs of superoxide within the O_2^-·BzOx cluster (Sec. 1).

As pointed out in Section 4.2, roots 2 and 3 in Figure 6 can be both thought of as the canonical π^* LUMO of BzOx coupled to the pseudocontinuum. Their divergent behaviors with the CAP onset are therefore notable. The continuum coupling results in two non-Hermitian states, one of which (root 3) is stabilized, while the other (root 2) is destabilized by the interaction.

4.4. Temporary anion states. Figures 8 and 9 summarize the CAP-induced evolution (the so-called η-trajectories)[53,97] of resonances A and B, respectively. The top part of each figure shows the changes in the Dyson orbitals originating from roots 3 (A) and 6 (B) in Figure 6. These changes illuminate the transformation of the CAP-free solutions ($\eta = 0$) into discrete resonances states.

As the CAP is turned on, the Dyson orbitals in Figures 8 and 9 acquire imaginary parts, represented by the purple and green plots next to their real (red and blue) components. The imaginary orbitals grow rapidly at first as η is increased from zero and then shrink slowly due to absorption by the CAP as η is increased further. The real parts of the orbitals also undergo changes with increasing η, but after a certain η value these changes become imperceptible, indicating that the resonance has been stabilized. The largest value of η chosen for the orbital plots in Figure 8 (resonance A) is $\eta = 0.006$ a.u. In Figure 9 (resonance B), it is $\eta = 0.018$ a.u., as the higher-energy resonance requires a greater degree of stabilization. Beyond these values, no changes to the real parts of the wave functions are perceptible to the eye, while the imaginary parts continue to shrink slowly until they vanish.

The bottom portions of Figures 8 and 9 depict the changes in the real and imaginary parts of the energy eigenvalues. Two types of $E(\eta)$ trajectories are plotted for each resonance, representing

the zeroth- and first-order values ('○' and '×', respectively). The first-order results include corrections for the CAP distortions as described below.[53-54] The energy scales are 0.20 eV wide for Re(E) and 0.10 eV wide for Im(E) in both figures. The equivalent widths are to make obvious the narrower energy range transversed by the $E(\eta)$ trajectory of resonance B (Figure 9) compared to A (Figure 8). The difference is not surprising since resonance B has a less diffuse continuum contribution (compare roots 3 and 6 in Figure 6) and is hence less affected by the CAP.

Since the CAP in Eq. 1 is an artificial construct, the true transient anion properties would be obtained in the $\eta \to 0$ limit—but only in the case of a complete basis.[111] With a finite basis, such as aug-cc-pVDZ+3p3d(C), an optimal finite value $\eta_{\text{opt}} > 0$ must be determined. It must be large enough to stabilize the resonance but not too large as to render its perturbed properties meaningless for chemists. The optimization is accomplished by minimizing the magnitude of logarithmic "velocity" along the η-trajectory, defined as:[54,97,111-112]

$$v(\eta) = \left|\eta \frac{dE(\eta)}{d\eta}\right| \tag{2}$$

Minimizing $v(\eta)$ for the zeroth-order $E(\eta)$ trajectory of resonance A (Figure 8) yields η_{opt} = 2.03×10^{-3} a.u. The corresponding resonance position is E_R = Re(E) = 0.900 eV, while the width is Γ = –2Im(E) = 0.069 eV. The resonance distortion due to the CAP is taken into account by the first-order correction to $E(\eta)$ equal to $-\eta \frac{dE}{d\eta}$ and then minimizing $v(\eta)$ in Eq. (2) for the corrected trajectory ('×' in Figures 8 and 9).[53-54] The first-order η_{opt} value for resonance A was found to be 4.00×10^{-3} a.u., corresponding to the corrected resonance position and width E_R = 0.891 eV and Γ = 0.072 eV. These results are summarized in Table 1.

CAP optimization proved to be challenging for resonance B. Its $E(\eta)$ trajectory is shallow over a broad range of η (Figure 9), and the $v(\eta)$ minimum is difficult to identify. However, since the energy variation is confined to a narrow range along the η-trajectory, we can assume an estimated

Re(E) value of 1.76 eV. All three significant figures in this determination are solid, based on the Re(E) trajectories in Figure 9, rendering the η_{opt} value moot as far as practical chemistry is concerned. The Im(E) value is similarly estimated in the −0.01 to −0.02 eV range, corresponding to a resonance width of 0.02–0.04 eV (Table 1).

4.5. Charge-transfer cluster states. The above theory predicts two low-lying temporary anion states of BzOx at 0.891 eV and 1.76 eV, respectively (Table 1). The predicted widths of these resonances reflect only their electronic lifetimes. Including the Franck-Condon profiles, significantly broader charge-transfer bands are expected in the experimental spectra.

Moreover, the above resonance energies were calculated for an isolated BzOx molecule. They do not include the interactions between the temporary $BzOx^-$ anion and neutral O_2 within the $O_2{\cdot}BzOx^-$ cluster. Like in the case of O_2^-·benzene and other similar clusters,[32,34-35,102] the neutral $O_2{\cdot}BzOx$ complex formed in $O_2^-{\cdot}BzOx$ cluster photodetachment is launched on the repulsive part of the neutral intermolecular (IM) potential. This implies that the $O_2{\cdot}BzOx$ states are destabilized by the IM forces relative to the O_2 + BzOx dissociation limit. To the contrary, the $O_2{\cdot}BzOx^-$ temporary anion states may be either stabilized by the ion-neutral interactions or slightly destabilized because the cluster geometry is optimized for the charge localized on the oxygen moiety. As a result, we expect the $O_2{\cdot}BzOx^-$ resonance positions to be vertically lower in energy with respect to the corresponding $O_2{\cdot}BzOx$ states, compared to an isolated benzoxazole molecule.

To estimate the effect of these interactions, we carried out several single-point CCSD and EOM-EA-CCSD calculations for the optimized $O_2^-{\cdot}BzOx$ cluster structure. The results are summarized in Figures 10 and 11. A detailed summary of all energetics is given in Table S1 in SI.

First, the vertical $O_2(^3\Sigma_g^-){\cdot}BzOx$ and $O_2(^1\Delta_g){\cdot}BzOx$ neutral-state energies determined from CCSD calculations are indicated in Figure 10 by green solid lines relative to the $O_2^-{\cdot}BzOx$ ground

state. Due to the repulsive nature of the neutral IM potentials, both neutral-cluster states lie higher in energy than their respective O_2 + BzOx dissociation limits, also indicated in the figure.

Second, CAP-EOM-EA-CCSD calculations similar to those in Section 4.4 were used to determine the $O_2(^3\Sigma_g^-,^1\Delta_g)$·BzOx$^-$(A,B) temporary-anion energies relative to the O_2^-·BzOx ground state. Here, BzOx$^-$(A) and BzOx$^-$(B) are the same anion resonances discussed in Section 4.4 but obtained by adding an electron to either the $O_2(^3\Sigma_g^-)$·BzOx (triplet) or the $O_2(^1\Delta_g)$·BzOx (singlet) neutral reference, as shown in Figure 11. The same aug-cc-pVDZ+3p3d(C) basis set and the same CAP onsets were used here as in Sections 4.1-4.4. Calculations of η-trajectories were not attempted in the cluster case. Instead, the zeroth-order η_{opt} value for resonance A from the BzOx-only calculations in Section 4.4 was used (η_{opt} = 0.002 a.u.). The resulting O_2·BzOx$^-$(A,B) resonance energies are indicated in Figure 10 (dotted lines). The Dyson orbitals for electron attachment to $O_2(^3\Sigma_g^-)$·BzOx and $O_2(^1\Delta_g)$·BzOx yielding the $O_2(^3\Sigma_g^-,^1\Delta_g)$·BzOx$^-$(A,B) temporary anions and the $O_2^-(^2\Pi_g)$·BzOx ground state are shown in Figure 11.

Based on these results, the $O_2(^1\Delta_g)$·BzOx$^-$(A) and $O_2(^3\Sigma_g^-)$·BzOx$^-$(B) temporary anion states lie 0.24 eV and 0.72 eV, respectively, below the 355 nm photon energy (3.495 eV). These estimates do not include the vibrational excitation of the O_2 and BzOx moieties upon the charge transfer between them. Therefore, we expect 355 nm photons to be resonant with a wide range of the $O_2(^1\Delta_g)$·BzOx$^-$(A) and $O_2(^3\Sigma_g^-)$·BzOx$^-$(B) states. These transitions correspond to electron transfer, respectively, from the bottom-right to the middle-right and from the bottom-left to the upper-left MOs in Figure 11 (with a caveat that these are Dyson rather than canonical orbitals). Upon decay of the temporary states, the emitted electrons match the energy gaps of the $O_2(^1\Delta_g)$·BzOx$^-$(A) → $O_2(^1\Delta_g)$·BzOx and $O_2(^3\Sigma_g^-)$·BzOx$^-$(B) → $O_2(^3\Sigma_g^-)$·BzOx transitions, indicated by the pink (0.47

eV) and blue (1.43 eV) block arrows in Figure 10. The $O_2(^1\Delta_g)\cdot BzOx^-$(A) and $O_2(^3\Sigma_g^-)\cdot BzOx^-$(B) temporary anions should therefore result in broad photoelectron bands in the 355 nm $O_2^-\cdot BzOx$ spectrum at eKE ≈ 0.47 eV and eKE ≈ 1.43 eV, respectively.

Similarly, the $O_2(^3\Sigma_g^-)\cdot BzOx^-$(A) resonance lies 0.28 eV below the 532 nm photon energy (Figure 10). Excitation of this resonance corresponds to electron transfer from the bottom-left to the middle-left MO in Figure 11 (the above caveat applies). The Franck-Condon profile of this transition ensures that 532 nm light is resonant with a range of the $O_2(^3\Sigma_g^-)\cdot BzOx^-$(A) vibrational levels. Autodetachment from these temporary states (0.56 eV purple block arrow in Figure 10) is expected to yield a broad band at eKE ≈ 0.56 eV.

5. Discussion

The autodetachment bands predicted in Section 4.5 are an excellent match to the "extra" signal in the $O_2^-\cdot BzOx$ photoelectron spectra unaccounted for by the direct photodetachment model in Figure 4(c) and (d).

Figure 4(e) shows a global simulation (red) of the 355 nm $O_2^-\cdot BzOx$ spectrum. It is obtained as a sum of the direct transitions in solvated O_2^- (green) and two charge-transfer autodetachment bands, A (pink) and B (blue). Similarly, Figure 4(f) shows a model simulation of the 532 nm spectrum obtained similarly as a sum of the direct transition (green) and charge-transfer band A (purple). For clarity, in both cases the charge-transfer model bands are scaled by 1/2 relative to the direct-detachment transitions.

The direct spectra represented by bold green dashed lines in Figures 4(e) and (f) are calculated as shifted and broadened Franck-Condon simulations of O_2^- photodetachment, similar to the red model spectra in Figures 4(a)-(d). The charge-transfer bands correspond to the two temporary-

anion states of benzoxazole, $BzOx^-$(A) and $BzOx^-$(B) from Section 4, coupled with O_2 in the ground $^3\Sigma_g^-$ or excited $^1\Delta_g$ states. These bands are assigned Gaussian profiles, and their positions, intensities, and widths are adjusted to match the experimental spectrum (details in SI).

Specifically, band A in Figure 4(e) is assigned to the O_2^-·BzOx → $O_2(^1\Delta_g)$·$BzOx^-$(A) charge-transfer transition. It is followed by autodetachment to the $O_2(^1\Delta_g)$·BzOx neutral complex which promptly dissociates to $O_2(^1\Delta_g)$ + BzOx. Band B in the same figure is due to the O_2^-·BzOx → $O_2(^3\Sigma_g^-)$·$BzOx^-$(B) charge-transfer transition, followed by autodetachment to $O_2(^3\Sigma_g^-)$·BzOx, yielding the $O_2(^3\Sigma_g^-)$ + BzOx dissociated products. Band A in Figure 4(f) is attributed to the O_2^-·BzOx → $O_2(^3\Sigma_g^-)$·$BzOx^-$(A) electron transfer, followed by decay to the $O_2(^3\Sigma_g^-)$·BzOx neutral state and the $O_2(^3\Sigma_g^-)$ + BzOx dissociated products.

The global model spectrum in Figure 4(e) assumes the resonance positions of eKE = 0.45 eV (A) and 1.52 eV (B). These transitions are in excellent agreement with the pink (0.47 eV) and blue (1.43 eV) block arrows in Figure 10. Similarly, band A in Figure 4(f) is centered at eKE = 0.48 eV, which is a good match to the purple block arrow in Figure 10 (0.56 eV). All resonance assignments and energies are summarized in Table 2.

Assuming a combination of direct photodetachment of solvated O_2^- with three charge-transfer transitions, specifically, O_2^-·BzOx → $O_2(^3\Sigma_g^-)$·$BzOx^-$(A), $O_2(^3\Sigma_g^-)$·$BzOx^-$(B), and $O_2(^1\Delta_g)$·$BzOx^-$(A), we are able to explain all observed features of the O_2^-·BzOx photoelectron spectra. These transitions involve the ground and excited electronic states of neutral O_2 and two low-lying anionic resonances (A and B) associated with the π MO system of benzoxazole.

We can also comment on the relative intensities of the direct (green) and charge-transfer (pink, purple, and blue) bands that contribute to the combined model spectra (solid red) in Figures 4(e)

and (f). The 355 nm spectrum (e) includes a 56% direct contribution, with the remaining 44% attributed to charge transfer followed by autodetachment (34% and 10% for $BzOx^-$ resonances A and B, respectively). Without commenting on the relative cross sections, the larger contribution of resonance A is consistent with the $O_2(^1\Delta_g)\cdot BzOx^-(A)$ electronic energy being closer to the 355 nm photon energy compared with the other, $O_2(^3\Sigma_g^-)\cdot BzOx^-(B)$, charge-transfer state (Figure 10).

In Figure 4(f), 85% of the 532 nm model spectrum intensity arises from the $O_2(^3\Sigma_g^-)\cdot BzOx^-(A)$ charge-transfer state. It is not surprising, therefore, that the direct-photodetachment model [Section 3.3 and Figure 4(d)] was not able to generate a passable resemblance of the 532 nm experimental spectrum. While autodetachment accounts for less than half of the 355 nm signal, the 532 nm spectrum is dominated by the $O_2^-\cdot BzOx \rightarrow O_2(^3\Sigma_g^-)\cdot BzOx^-(A)$ charge-transfer transition.

6. Conclusion

The photoelectron spectra of the $O_2^-\cdot BzOx$ cluster anion reveal two competing photodetachment processes: a direct photoemission from the solvated O_2^- cluster core and an indirect charge-transfer pathway involving temporary anion states of benzoxazole. Although benzoxazole does not form permanent anions, its low-lying vacant π* orbitals permit a resonant capture of the electron emitted from the cluster core.

The non-Hermitian theory using a complex absorbing potential predicts the existence of two $BzOx^-$ π* resonances within the experimental energy range: resonance A at 0.891 eV and resonance B at 1.76 eV, relative to the onset of the $BzOx + e^-$ continuum at the ground-state geometry of neutral BzOx. Within the clusters, the temporary $O_2\cdot BzOx^-$ charge-transfer states are partially stabilized relative to the free-electron limit by interactions with neutral O_2. These interactions depend on the electronic states of both species. The theory predicts that, at the $O_2^-\cdot BzOx$ cluster

geometry, the $O_2(X^3\Sigma_g^-)\cdot BzOx^-(A)$ and $O_2(a^1\Delta_g)\cdot BzOx^-(A)$ states lie at 0.56 eV and 0.47 eV (vertically) above the respective neutral states. The $O_2(^3\Sigma_g^-)\cdot BzOx^-(B)$ resonance is found 1.43 eV (vertically) above $O_2(X^3\Sigma_g^-)\cdot BzOx$. Signatures of both $BzOx^-$ resonances, A and B, and the three abovementioned charge-transfer states, $O_2(X^3\Sigma_g^-)\cdot BzOx^-(A)$, $O_2(a^1\Delta_g)\cdot BzOx^-(A)$ and $O_2(^3\Sigma_g^-)\cdot BzOx^-(B)$, are observed in the 355 nm (3.495 eV) and 532 nm (2.330 eV) photoelectron spectra of the $O_2^-\cdot BzOx$ cluster anion. Other temporary charge-transfer states are expected, including the $BzOx^-(B)$ resonance paired with the $a^1\Delta_g$ state of O_2, and the A and B anionic resonances of benzoxazole each paired with $O_2(b^1\Sigma_g^+)$, but these states lie outside the experimental energy range.

The temporary anion states activated in the charge-transfer mechanism, rather than direct photodetachment from solvated O_2^-, account for nearly a half of the $O_2^-\cdot BzOx$ cluster photodetachment intensity at 355 nm and for most of the signal observed at 532 nm. Therefore, only by including these solvent-based resonances in the analysis is it possible to model and interpret the experimental results.

Looking forward, a clearer picture of these resonances may be obtained by using atomic anions as initial electron sources with narrow eKE distributions, instead of molecular species such as superoxide. Additional information can also be obtained by measuring two-dimensional photoelectron spectra obtained by scanning the photon energy over the resonance range.[16,19-20]

ASSOCIATED CONTENT

Supporting Information

The Supporting Information is available free of charge at https://pubs.acs.org/doi/10.1021/acs.jpca.XXXX

The Supporting Information includes the relaxed geometries of benzoxazole and the $O_2^-\cdot BzOx$ cluster anion; details of the photodetachment energetics summarized in Figure 10; and details of

the spectral simulations presented in Figures 3 and 4.

AUTHOR INFORMATION

Corresponding Author

*Email: sanov@arizona.edu

ORCID

Beverly Feng: 0000-0003-1258-6224

Sydney Cordova: 0009-0002-6803-4621

Connor Fang: 0009-0001-1001-0136

Andrei Sanov: 0000-0002-2373-4387

Funding Sources

U.S. National Science Foundation Grant CHE-2153986.

Notes

The authors declare no competing financial interest.

ACKNOWLEDGMENTS

This research is supported by the U.S. National Science Foundation through grant CHE-2153986.

Table 1. Benzoxazole anion resonance properties determined from the CAP-EOM-EA-CCSD calculations.

	Resonance A		Resonance B
	0^{th} order	1^{st} order	(estimated)
η_{opt} / a.u.	2.03×10^{-3}	4.00×10^{-3}	n/a
$v(\eta_{opt})$ / a.u.	2.85×10^{-4}	1.00×10^{-4}	n/a
E_R / eV	0.900	0.891	1.76
Γ / eV	0.069	0.072	0.02–0.04

Table 2. Spectral assignments and electron kinetic energies (in eV) of the observed charge-transfer bands.

	Figure	Charge-transfer state	Theory	Experiment
355 nm Band A	4(e)	$O_2(^1\Delta_g)\cdot BzOx^-(A)$	0.47	0.45
355 nm Band B	4(e)	$O_2(^3\Sigma_g^-)\cdot BzOx^-(B)$	1.43	1.52
532 nm Band A	4(f)	$O_2(^3\Sigma_g^-)\cdot BzOx^-(A)$	0.56	0.48

References

1. Mason, N. J.; Nair, B.; Jheeta, S.; Szymańska, E., Electron induced chemistry: a new frontier in astrochemistry. *Faraday Discuss.* **2014,** *168*, 235-247.
2. Simons, J., How Do Low-Energy (0.1−2 eV) Electrons Cause DNA-Strand Breaks? *Acc. Chem. Res.* **2006,** *39*, 772-779.
3. Graupner, K.; Field, T. A.; Saunders, G. C., Experimental Evidence for Radiative Attachment in Astrochemistry from Electron Attachment to NCCCCN. *Astrophys. J.* **2008,** *685*, L95.
4. Masui, H.; Ho, Y. K., Resonance states with the complex absorbing potential method. *Phys. Rev. C* **2002,** *65*, 054305.
5. Zuev, D.; Bravaya, K. B.; Crawford, T. D.; Lindh, R.; Krylov, A. I., Electronic structure of the two isomers of the anionic form of p-coumaric acid chromophore. *J. Chem. Phys.* **2011,** *134*, 034310.
6. Jordan, K. D.; Michejda, J. A.; Burrow, P. D., A study of the negative ion states of selected cyclodienes by electron transmission spectroscopy. *Chem. Phys. Lett.* **1976,** *42*, 227-231.
7. Jordan, K. D.; Burrow, P. D., Studies of the temporary anion states of unsaturated hydrocarbons by electron transmission spectroscopy. *Acc. Chem. Res.* **1978,** *11*, 341-348.
8. Burrow, P. D.; Modelli, A.; Chiu, N. S.; Jordan, K. D., Temporary negative ions in the chloromethanes $CHCl_2F$ and CCl_2F_2: Characterization of the σ* orbitals. *J. Chem. Phys.* **1982,** *77*, 2699-2701.
9. Burrow, P. D.; Michejda, J. A.; Jordan, K. D., Electron transmission study of the temporary negative ion states of selected benzenoid and conjugated aromatic hydrocarbons. *J. Chem. Phys.* **1987,** *86*, 9-24.
10. Modelli, A.; Burrow, P. D., Electron attachment to the aza-derivatives of furan, pyrrole, and thiophene. *J. Phys. Chem. A* **2004,** *108*, 5721-5726.
11. Jordan, K. D.; Burrow, P. D., Temporary Anion States of Polyatomic Hydrocarbons. *Chem. Rev.* **1987,** *87*, 557-588.
12. Velarde, L.; Habteyes, T.; Grumbling, E. R.; Pichugin, K.; Sanov, A., Solvent resonance effect on the anisotropy of $NO^-(N_2O)_n$ cluster anion photodetachment. *J. Chem. Phys.* **2007,** *127*, 084302.
13. West, C. W.; Bull, J. N.; Antonkov, E.; Verlet, J. R. R., Anion Resonances of para-Benzoquinone Probed by Frequency-Resolved Photoelectron Imaging. *J. Phys. Chem. A* **2014,** *118*, 11346-11354.
14. Jagau, T. C.; Dao, D. B.; Holtgrewe, N. S.; Krylov, A. I.; Mabbs, R., Same but Different: Dipole-Stabilized Shape Resonances in CuF and AgF. *J. Phys. Chem. Lett.* **2015,** *6*, 2786-2793.
15. Lyle, J.; Jagau, T. C.; Mabbs, R., Spectroscopy of temporary anion states: Renner-Teller coupling and electronic autodetachment in copper difluoride anion. *Faraday Discuss.* **2019,** *217*, 533-546.
16. Lietard, A.; Mensa-Bonsu, G.; Verlet, J. R. R., The effect of solvation on electron capture revealed using anion two-dimensional photoelectron spectroscopy. *Nature Chemistry* **2021,** *13*, 737-742.
17. Cooper, G. A.; Clarke, C. J.; Verlet, J. R. R., Electron impact resonances of uracil in an aqueous environment from anion photoelectron imaging. *J. Phys. B* **2023,** *56*, 185102.
18. Rankovic, M.; Nag, P.; Anstöter, C. S.; Mensa-Bonsu, G.; Kumar, T. P. R.; Verlet, J. R. R.; Fedor, J., Resonances in nitrobenzene probed by the electron attachment to neutral and by

the photodetachment from anion. *J. Chem. Phys.* **2022,** *157*, 064302.
19. Lietard, A.; Verlet, J. R. R.; Slimak, S.; Jordan, K. D., Temporary Anion Resonances of Pyrene: A 2D Photoelectron Imaging and Computational Study. *J. Phys. Chem. A* **2021,** *125*, 7004-7013.
20. Hart, C. A.; Schlimgen, A. W.; Dao, D. B.; Head-Marsden, K.; Mabbs, R., The overlooked role of excited anion states in NiO^- photodetachment. *J. Chem. Phys.* **2024,** *160*, 044304.
21. Johnson, M. A.; Lineberger, W. C., Pulsed Methods for Cluster Ion Spectroscopy. In *Techniques for the Study of Ion Molecule Reactions*, Farrar, J. M.; Saunders, W. H., Eds. Wiley: New York, 1988; pp 591-635.
22. Castleman, A. W.; Bowen, K. H., Clusters: Structure, Energetics, and Dynamics of Intermediate States of Matter. *J. Phys. Chem.* **1996,** *100*, 12911-12944.
23. Dermota, T. E.; Zhong, Q.; Castleman, A. W., Ultrafast Dynamics in Cluster Systems. *Chem. Rev.* **2004,** *104*, 1861-1886.
24. Sanov, A.; Lineberger, W. C., Cluster anions: Structure, interactions, and dynamics in the sub-nanoscale regime. *Phys. Chem. Chem. Phys.* **2004,** *6*, 2018-2032.
25. Shin, J. W.; Hammer, N. I.; Johnson, M. A.; Schneider, H.; Gloss, A.; Weber, J. M., An infrared investigation of the $(CO_2)_n^-$ clusters: Core ion switching from both the ion and solvent perspectives. *J. Phys. Chem. A* **2005,** *109*, 3146-3152.
26. Sanov, A., Intermolecular interactions in cluster anions. *Int. Rev. Phys. Chem.* **2021,** *40*, 495-545.
27. Neumark, D. M., Spectroscopy of Radicals, Clusters, and Transition States Using Slow Electron Velocity-Map Imaging of Cryogenically Cooled Anions. *J. Phys. Chem. A* **2023,** *127*, 4207-4223.
28. Ervin, K. M.; Lineberger, W. C., Photoelectron Spectroscopy of Negative Ions. In *Advances in Gas Phase Ion Chemistry*, Adams, N. G.; Babcock, L. M., Eds. JAI Press: Greenwich, 1992; Vol. 1, pp 121-166.
29. Kloepfer, J. A.; Vilchiz, V. H.; Lenchenkov, V. A.; Bradforth, S. E., Femtosecond dynamics of photodetachment of the iodide anion in solution: resonant excitation into the charge-transfer-to-solvent state. *Chem. Phys. Lett.* **1998,** *298*, 120-128.
30. Mabbs, R.; Surber, E.; Sanov, A., Photoelectron anisotropy and channel branching ratios in the detachment of solvated iodide cluster anions. *J. Chem. Phys.* **2005,** *122*, 054308.
31. Grumbling, E. R.; Pichugin, K.; Velarde, L.; Sanov, A., Further evidence for resonant photoelectron-solvent scattering in nitrous oxide cluster anions. *J. Phys. Chem. A* **2010,** *114*, 1367-1373.
32. Patros, K. M.; Mann, J. E.; Jarrold, C. C., Photoelectron Imaging Spectra of $O_2^-\cdot$VOC and $O_4^-\cdot$VOC Complexes. *J. Phys. Chem. A* **2016,** *120*, 7828-7838.
33. Nakanishi, R.; Muraoka, A.; Nagata, T., Photoelectron spectroscopy of acetone cluster anions, $[(CH_3)_2CO]_n^-$ (n = 2, 5-15). *Chem. Phys. Lett.* **2006,** *427*, 56-61.
34. Dobulis, M. A.; Thompson, M. C.; Sommerfeld, T.; Jarrold, C. C., Temporary anion states of fluorine substituted benzenes probed by charge transfer in $O_2^-\cdot C_6H_{6-x}F_x$ (x = 0–5) ion–molecule complexes. *J. Chem. Phys.* **2020,** *152*, 204309.
35. Davis, J. U.; Jarrold, C. C.; Sommerfeld, T., Charge distribution in oxygen-fluorobenzene complex anions $[O_2\bullet C_6H_{6-n}F_n]^-$ (n = 0-6). *Chem. Phys.* **2023,** *574*, 112023.
36. Sanche, L.; Schulz, G. J., Electron Transmission Spectroscopy - Resonances in Triatomic Molecules and Hydrocarbons. *J. Chem. Phys.* **1973,** *58*, 479-493.
37. Wong, X. K.; Yeong, K. Y., A Patent Review on the Current Developments of Benzoxazoles

in Drug Discovery. *ChemMedChem* **2021,** *16*, 3237-3262.
38. Kakkar, S.; Kumar, S.; Narasimhan, B.; Lim, S. M.; Ramasamy, K.; Mani, V.; Shah, S. A. A., Design, synthesis and biological potential of heterocyclic benzoxazole scaffolds as promising antimicrobial and anticancer agents. *Chem. Cent. J.* **2018,** *12*, 96.
39. Kakkar, S.; Tahlan, S.; Lim, S. M.; Ramasamy, K.; Mani, V.; Shah, S. A. A.; Narasimhan, B., Benzoxazole derivatives: design, synthesis and biological evaluation. *Chem. Cent. J.* **2018,** *12*, 92.
40. Sattar, R.; Mukhtar, R.; Atif, M.; Hasnain, M.; Irfan, A., Synthetic transformations and biological screening of benzoxazole derivatives: A review. *J. Heterocycl. Chem.* **2020,** *57*, 2079-2107.
41. Angajala, G.; Subashini, R., Synthesis, molecular modeling, and pharmacological evaluation of new 2-substituted benzoxazole derivatives as potent anti-inflammatory agents. *Struct. Chem.* **2020,** *31*, 263-273.
42. Ervin, K. M.; Anusiewicz, W.; Skurski, P.; Simons, J.; Lineberger, W. C., The only stable state of O_2^- is the X $^2\Pi_g$ ground state and it (still!) has an adiabatic electron detachment energy of 0.45 eV. *J. Phys. Chem. A* **2003,** *107*, 8521-8529.
43. Buntine, M. A.; Lavrich, D. J.; Dessent, C. E.; Scarton, M. G.; Johnson, M. A., Photoinitiation of the $O^- + H_2O \rightarrow OH^- + OH$ Ion-Molecule Reaction within the $O_2^-{\cdot}H_2O$ Binary Complex. *Chem. Phys. Lett.* **1993,** *216*, 471-478.
44. Sherwood, C. R.; Continetti, R. E., Dissociative photodetachment dynamics of $O_2^-{\cdot}(H_2O)$. *Chem. Phys. Lett.* **1996,** *258*, 171-179.
45. Luong, A. K.; Clements, T. G.; Resat, M. S.; Continetti, R. E., Energetics and dissociative photodetachment dynamics of superoxide-water clusters: $O_2^-(H_2O)_n$, n =1-6. *J. Chem. Phys.* **2001,** *114*, 3449-3455.
46. Weber, J. M.; Kelley, J. A.; Robertson, W. H.; Johnson, M. A., Hydration of a structured excess charge distribution: Infrared spectroscopy of the $O_2^-{\cdot}(H_2O)_n$, $(1 \le n \le 5)$ clusters. *J. Chem. Phys.* **2001,** *114*, 2698-2706.
47. Akin, F. A.; Schirra, L. K.; Sanov, A., Photoelectron imaging study of the effect of monohydration on O_2^- photodetachment. *J. Phys. Chem. A* **2006,** *110*, 8031-8036.
48. Goebbert, D. J.; Sanov, A., Photodetachment, photofragmentation, and fragment autodetachment of $[O_{2n}(H_2O)_m]^-$ clusters: Core-anion structures and fragment energy partitioning. *J. Chem. Phys.* **2009,** *131*, 104308.
49. Krylov, A. I., From orbitals to observables and back. *J. Chem. Phys.* **2020,** *153*, 080901.
50. Ortiz, J. V., Dyson-orbital concepts for description of electrons in molecules. *J. Chem. Phys.* **2020,** *153*, 070902.
51. Moitra, T.; Ponzi, A.; Koch, H.; Coriani, S.; Decleva, P., Accurate Description of Photoionization Dynamical Parameters. *J. Phys. Chem. Lett.* **2020,** *11*, 5330-5337.
52. Díaz–Tinoco, M.; Corzo, H. H.; Pawłowski, F.; Ortiz, J. V., Do Dyson Orbitals resemble canonical Hartree–Fock orbitals? *Mol. Phys.* **2019,** *117*, 2275-2283.
53. Jagau, T.-C.; Zuev, D.; Bravaya, K. B.; Epifanovsky, E.; Krylov, A. I., A Fresh Look at Resonances and Complex Absorbing Potentials: Density Matrix-Based Approach. *J. Phys. Chem. Lett.* **2014,** *5*, 310-315.
54. Jagau, T.-C.; Krylov, A. I., Characterizing metastable states beyond energies and lifetimes: Dyson orbitals and transition dipole moments. *J. Chem. Phys.* **2016,** *144*, 054113.
55. Surber, E.; Ananthavel, S. P.; Sanov, A., Nonexistent electron affinity of OCS and the stabilization of carbonyl sulfide anions by gas phase hydration. *J. Chem. Phys.* **2002,** *116*,

1920-1929.
56. Surber, E.; Sanov, A., Photoelectron imaging spectroscopy of molecular and cluster anions: CS_2^- and $OCS^-(H_2O)_{1,2}$. *J. Chem. Phys.* **2002,** *116*, 5921-5924.
57. Mabbs, R.; Surber, E.; Sanov, A., Photoelectron Imaging of Negative Ions: Atomic Anions to Molecular Clusters. *Analyst* **2003,** *128*, 765-772.
58. Ru, B.; Sanov, A., Photoelectron Spectra of Hot Polyatomic Ions: A Statistical Treatment of Phenide. *J. Phys. Chem. A* **2022,** *126*, 9423-9439.
59. Blackstone, C. C. Exploring the Chemistry of Methoxide with Oxygen Through Photoelectron Imaging Spectroscopy. Ph.D. dissertation, University of Arizona, Tucson, 2020.
60. Feng, B.; Sanov, A., Microsolvation of Hot Ions: Spectroscopy and Statistical Mechanics of Phenide–Water Interactions. *J. Phys. Chem. A* **2023,** *127*, 6437-6446.
61. Wiley, W. C.; McLaren, I. H., Time-of-Flight Mass Spectrometer with Improved Resolution. *Rev. Sci. Instrum.* **1955,** *26*, 1150.
62. Arshadi, M.; Kebarle, P., Hydration of OH^- and O_2^- in the gas phase. Comparative solvation of OH^- by water and the hydrogen halides. Effects of acidity. *J. Phys. Chem.* **1970,** *74*, 1483-1485.
63. Adams, N. G.; Bohme, D. K.; Dunkin, D. B.; Fehsenfeld, F. C.; Ferguson, E. E., Flowing Afterglow Studies of Formation and Reactions of Cluster Ions of O_2^+, O_2^-, and O^-. *J. Chem. Phys.* **1970,** *52*, 3133-&.
64. Posey, L. A.; DeLuca, M. J.; Johnson, M. A., Demonstration of a Pulsed Photoelectron Spectrometer on Mass-Selected Negative Ions: O^-, O_2^-, and O_4^-. *Chem. Phys. Lett.* **1986,** *131*, 170-174.
65. Hiraoka, K., A determination of the stabilities of $O_2^+(O_2)_n$ and $O_2^-(O_2)_n$ with n=1-8 from measurements of the gas-phase ion equilibria. *J. Chem. Phys.* **1988,** *89*, 3190-3194.
66. DeLuca, M. J.; Han, C.-C.; Johnson, M. A., Photoabsorption of negative cluster ions near the electron detachment threshold: A Study of the $(O_2)_n^-$ system. *J. Chem. Phys.* **1990,** *93*, 268-75.
67. Han, C. C.; Johnson, M. A., Nascent vibrational distribution of the O_2^- product ion in the photodissociation of $(O)_n^-$, n = 2-4. *Chem. Phys. Lett.* **1992,** *189*, 460-466.
68. Lavrich, D. J.; Buntine, M. A.; Serxner, D.; Johnson, M. A., Excess Energy-Dependent Photodissociation Probabilities for O_2^- In Water Clusters: $O_2^-\cdot(H_2O)_N$, $1 \le N \le 33$. *J. Phys. Chem.* **1995,** *99*, 8453-8457.
69. Sherwood, C. R.; Garner, M. C.; Hanold, K. A.; Strong, K. M.; Continetti, R. E., Energy and Angular Distributions in Dissociative Photodetachment of O_4^-. *J. Chem. Phys.* **1995,** *102*, 6949-6952.
70. Sherwood, C. R.; Hanold, K. A.; Garner, M. C.; Strong, K. M.; Continetti, R. E., Translational Spectroscopy Studies of the Photodissociation Dynamics of O_4^-. *J. Chem. Phys.* **1996,** *105*, 10803-10811.
71. Hanold, K. A.; Garner, M. C.; Continetti, R. E., Photoelectron-Photofragment Angular-Correlation and Energy Partitioning in Dissociative Photodetachment. *Phys. Rev. Lett.* **1996,** *77*, 3335-3338.
72. Li, R. J.; Hanold, K. A.; Garner, M. C.; Luong, A. K.; Continetti, R. E., Excited state dynamics in clusters of oxygen. *Faraday Discuss.* **1997,** *108*, 115-130.
73. Hanold, K. A.; Continetti, R. E., Photoelectron-photofragment coincidence studies of the dissociative photodetachment of O_4^-. *Chem. Phys.* **1998,** *239*, 493-509.

74. Hanold, K. A.; Luong, A. K.; Continetti, R. E., Complete kinematic measurement of three-body reaction dynamics: Dissociative photodetachment of O_6^- at 532 nm. *J. Chem. Phys.* **1998,** *109*, 9215-9218.
75. Clements, T. G.; Continetti, R. E., Four-body reaction dynamics: Complete correlated fragment measurement of the dissociative photodetachment dynamics of O_8^-. *Phys. Rev. Lett.* **2002,** *89*, 033005.
76. Khuseynov, D.; Goebbert, D. J.; Sanov, A., Oxygen cluster anions revisited: Solvent-mediated dissociation of the core O_4^- anion. *J. Chem. Phys.* **2012,** *136*, 094312.
77. Wenthold, P. G.; Hu, J.; Squires, R. R., Regioselective Synthesis of Biradical Negative-Ions in the Gas-Phase: Generation of Trimethylenemethane, *m*-Benzyne, and *p*-Benzyne Anions. *J. Am. Chem. Soc.* **1994,** *116*, 6961-6962.
78. Wenthold, P. G.; Hu, J.; Squires, R. R., *o*-, *m*-, and *p*-benzyne negative ions in the gas phase: Synthesis, authentication, and thermochemistry. *J. Am. Chem. Soc.* **1996,** *118*, 11865-11871.
79. Wenthold, P. G.; Squires, R. R.; Lineberger, W. C., Ultraviolet Photoelectron Spectroscopy of the *o*-, *m*-, and *p*-Benzyne Negative Ions. Electron Affinities and Singlet−Triplet Splittings for *o*-, *m*-, and *p*-Benzyne. *J. Am. Chem. Soc.* **1998,** *120*, 5279-5290.
80. Wenthold, P. G.; Hu, J.; Squires, R. R., Gas-phase reactions of the benzyne negative ions. *J. Mass Spectrom.* **1998,** *33*, 796-802.
81. Eppink, A. T. J. B.; Parker, D. H., Velocity map imaging of ions and electrons using electrostatic lenses: Application in photoelectron and photofragment ion imaging of molecular oxygen. *Rev. Sci. Instrum.* **1997,** *68*, 3477-3484.
82. Chandler, D. W.; Houston, P. L., Two-Dimensional Imaging of State-Selected Photodissociation Products Detected by Multiphoton Ionization. *J. Chem. Phys.* **1987,** *87*, 1445-1447.
83. Heck, A. J. R.; Chandler, D. W., Imaging Techniques For the Study of Chemical Reaction Dynamics. *Annu. Rev. Phys. Chem.* **1995,** *46*, 335-372.
84. Surber, E.; Mabbs, R.; Sanov, A., Probing the electronic structure of small molecular anions by photoelectron imaging. *J. Phys. Chem. A* **2003,** *107*, 8215-8224.
85. Dribinski, V.; Ossadtchi, A.; Mandelshtam, V. A.; Reisler, H., Reconstruction of abel-transformable images: The Gaussian basis-set expansion abel transform method. *Rev. Sci. Instrum.* **2002,** *73*, 2634-2642.
86. Franck, J.; Dymond, E. G., Elementary processes of photochemical reactions. *Trans. Faraday Soc.* **1926,** *21*, 536-542.
87. Condon, E., A Theory of Intensity Distribution in Band Systems. *Phys. Rev.* **1926,** *28*, 1182-1201.
88. Condon, E. U., The Franck-Condon Principle and Related Topics. *Am. J. Phys.* **1947,** *15*, 365-374.
89. Parigger, C. G.; Hornkohl, J. O., Quantum Mechanics of the Diatomic Molecule with Applications. IOP Publishing: 2019. https://dx.doi.org/10.1088/978-0-7503-1989-8.
90. Wigner, E. P., On the behavior of cross sections near thresholds. *Phys. Rev.* **1948,** *73*, 1002-1009.
91. Sanov, A., Laboratory-Frame Photoelectron Angular Distributions in Anion Photodetachment: Insight into Electronic Structure and Intermolecular Interactions. *Annu. Rev. Phys. Chem.* **2014,** *65*, 341-363.
92. Engelking, P. C., Strong electron-dipole coupling in photodetachment of molecular negative ions: Anomalous rotational thresholds. *Phys. Rev. A* **1982,** *26*, 740-745.

93. Lakhmanskaya, O.; Simpson, M.; Murauer, S.; Kokoouline, V.; Wester, R., Photodetachment spectroscopy of cold trapped NH_2^- near threshold. *J. Chem. Phys.* **2018,** *149*, 104302.
94. Simpson, M.; Nötzold, M.; Schmidt-May, A.; Michaelsen, T.; Bastian, B.; Meyer, J.; Wild, R.; Gianturco, F. A.; Milovanović, M.; Kokoouline, V., et al., Threshold photodetachment spectroscopy of the astrochemical anion CN^-. *J. Chem. Phys.* **2020,** *153*, 184309.
95. Dauletyarov, Y.; Ru, B.; Sanov, A., Anion of Oxalyl Chloride: Structure and Spectroscopy. *J. Phys. Chem. A* **2021,** *125*, 9865-9876.
96. Climen, B.; Pagliarulo, F.; Ollagnier, A.; Baguenard, B.; Concina, B.; Lebeault, M. A.; Lépine, F.; Bordas, C., Threshold laws in delayed emission: an experimental approach. *Eur. Phys. J. D* **2007,** *43*, 85-89.
97. Zuev, D.; Jagau, T.-C.; Bravaya, K. B.; Epifanovsky, E.; Shao, Y.; Sundstrom, E.; Head-Gordon, M.; Krylov, A. I., Complex absorbing potentials within EOM-CC family of methods: Theory, implementation, and benchmarks. *J. Chem. Phys.* **2014,** *141*, 024102.
98. Sneskov, K.; Christiansen, O., Excited state coupled cluster methods. *Wiley Interdiscip. Rev.: Comput. Mol. Sci.* **2012,** *2*, 566-584.
99. Epifanovsky, E.; Gilbert, A. T. B.; Feng, X.; Lee, J.; Mao, Y.; Mardirossian, N.; Pokhilko, P.; White, A. F.; Coons, M. P.; Dempwolff, A. L., et al., Software for the frontiers of quantum chemistry: An overview of developments in the Q-Chem 5 package. *J. Chem. Phys.* **2021,** *155*, 084801.
100. Mabbs, R.; Mbaiwa, F.; Wei, J.; Van Duzor, M.; Gibson, S. T.; Cavanagh, S. J.; Lewis, B. R., Observation of vibration-dependent electron anisotropy in O_2^- photodetachment. *Phys. Rev. A* **2010,** *82*, 011401.
101. Van Duzor, M.; Mbaiwa, F.; Wei, J.; Singh, T.; Mabbs, R.; Sanov, A.; Cavanagh, S. J.; Gibson, S. T.; Lewis, B. R.; Gascooke, J. R., Vibronic coupling in the superoxide anion: The vibrational dependence of the photoelectron angular distribution. *J. Chem. Phys.* **2010,** *133*, 174311.
102. Patros, K. M.; Mann, J. E.; Jarrold, C. C., O_2^-·[Polar VOC] Complexes: H-Bonding versus Charge–Dipole Interactions, and the Noninnocence of Formaldehyde. *J. Phys. Chem. A* **2017,** *121*, 5459-5467.
103. Lin, P.; Lucchese, R. R., Studies of angular distributions and cross sections for photodetachment from the oxygen molecular anion. *J. Chem. Phys.* **2001,** *114*, 9350-9360.
104. Mason, J. L.; Topolski, J. E.; Ewigleben, J.; Iyengar, S. S.; Jarrold, C. C., Photoelectrons Are Not Always Quite Free. *J. Phys. Chem. Lett.* **2019,** *10*, 144-149.
105. Jarrold, C. C., Probing Anion–Molecule Complexes of Atmospheric Relevance Using Anion Photoelectron Detachment Spectroscopy. *ACS Phys. Chem. Au* **2023,** *3*, 17-29.
106. Schuchardt, K. L.; Didier, B. T.; Elsethagen, T.; Sun, L. S.; Gurumoorthi, V.; Chase, J.; Li, J.; Windus, T. L., Basis set exchange: A community database for computational sciences. *J Chem Inf Model* **2007,** *47*, 1045-1052.
107. Pritchard, B. P.; Altarawy, D.; Didier, B.; Gibson, T. D.; Windus, T. L., New Basis Set Exchange: An Open, Up-to-Date Resource for the Molecular Sciences Community. *J Chem Inf Model* **2019,** *59*, 4814-4820.
108. Levine, I. N., *Quantum Chemistry*. 5th ed.; Prentice-Hall: Upper Saddle River, NJ, 2000.
109. Moiseyev, N., *Non-Hermitian Quantum Mechanics*. Cambridge University Press: Cambridge, 2011.
110. Hazi, A. U.; Taylor, H. S., Stabilization Method of Calculating Resonance Energies: Model

Problem. *Phys. Rev. A* **1970,** *1*, 1109-1120.
111. Riss, U. V.; Meyer, H. D., Calculation of Resonance Energies and Widths Using the Complex Absorbing Potential Method. *J. Phys. B* **1993,** *26*, 4503-4536.
112. Riss, U. V.; Meyer, H. D., Reflection-Free Complex Absorbing Potentials. *J. Phys. B* **1995,** *28*, 1475-1493.

Figure 1

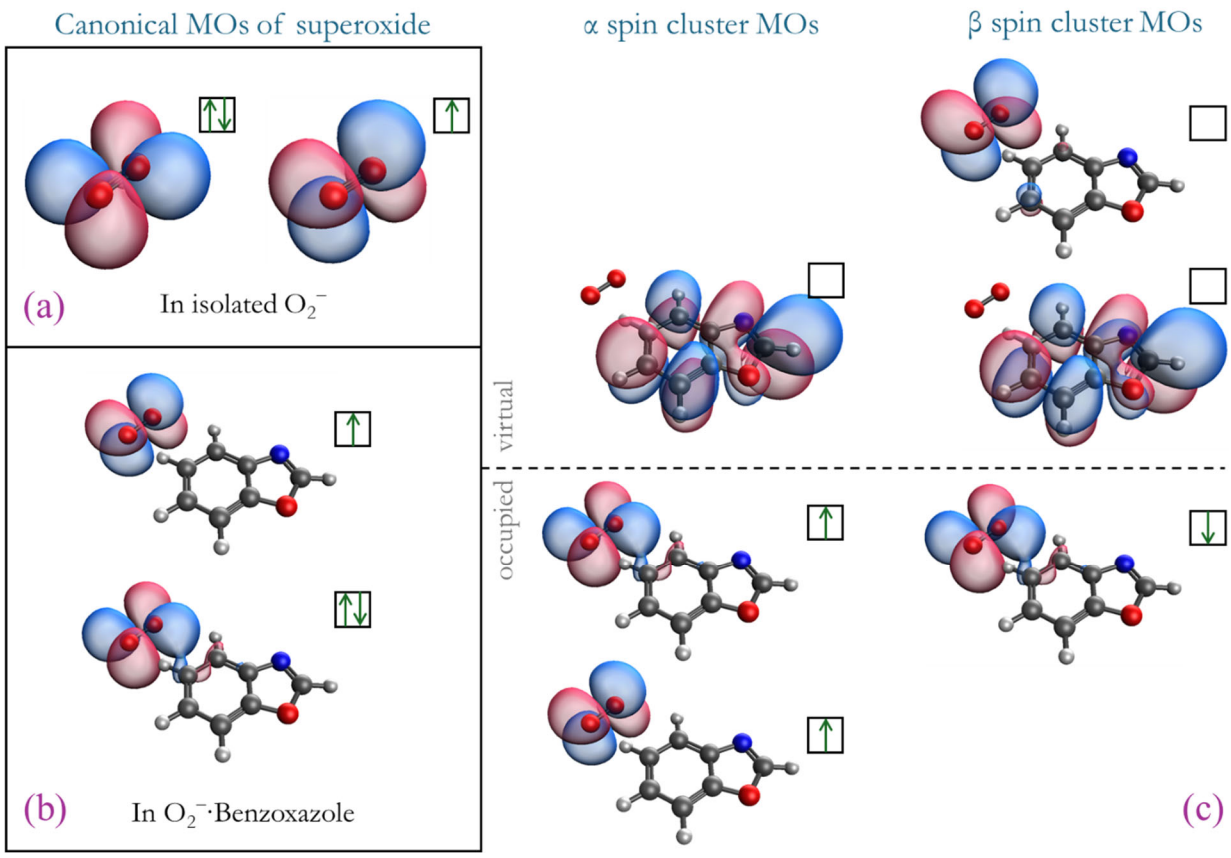

Figure 1. The molecular orbitals involved in the lowest-energy O_2^-·BzOx → O_2·$BzOx^-$ charge-transfer transitions. A spin-restricted view of the canonical HOMOs of isolated and solvated O_2^- is presented in parts (a) and (b), respectively. The unrestricted O_2^- HOMOs and BzOx LUMOs within the O_2^-·BzOx cluster are shown in (c). All orbitals are from B3LYP/aug-cc-pVDZ calculations and plotted at the 0.016 a.u. isosurface value.

Figure 2

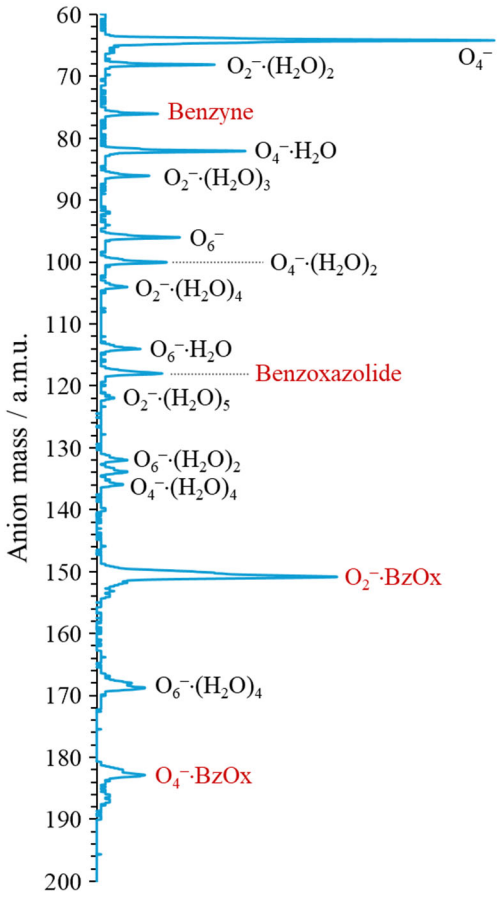

Figure 2. Representative negative-ion mass spectrum obtained using the benzoxazole precursor mixed with O_2 as the carrier gas.

Figure 3

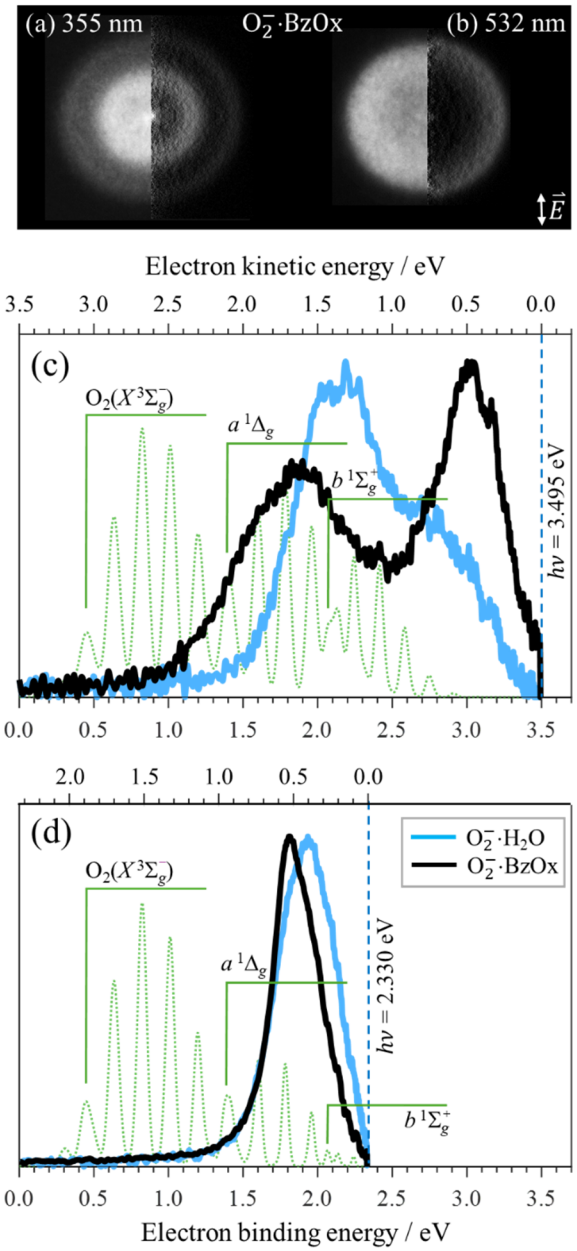

Figure 3. Top: the photoelectron images of O_2^-·BzOx obtained with (a) 355 nm (3.495 eV) and (b) 532 nm (2.330 eV) light. The left and right halves of the composite images are the raw and Abel-inverted data, respectively. The laser polarization direction is indicated by the double-arrow in (b). (c) Bold black: the 355 nm photoelectron spectrum of O_2^-·BzOx obtained from image (a) at the top of the figure. Bold blue: the O_2^-·H_2O spectrum obtained under similar experimental conditions. Dotted green: a Franck-Condon simulation of the unsolvated O_2^- spectrum under the same conditions. The origins of the $X\,^3\Sigma_g^-$, $a\,^1\Delta_g$, and $b\,^1\Sigma_g^+$ electronic states of neutral O_2 are indicated by the respective brackets. (d) Same as (c) but for the 532 nm laser wavelength.

Figure 4

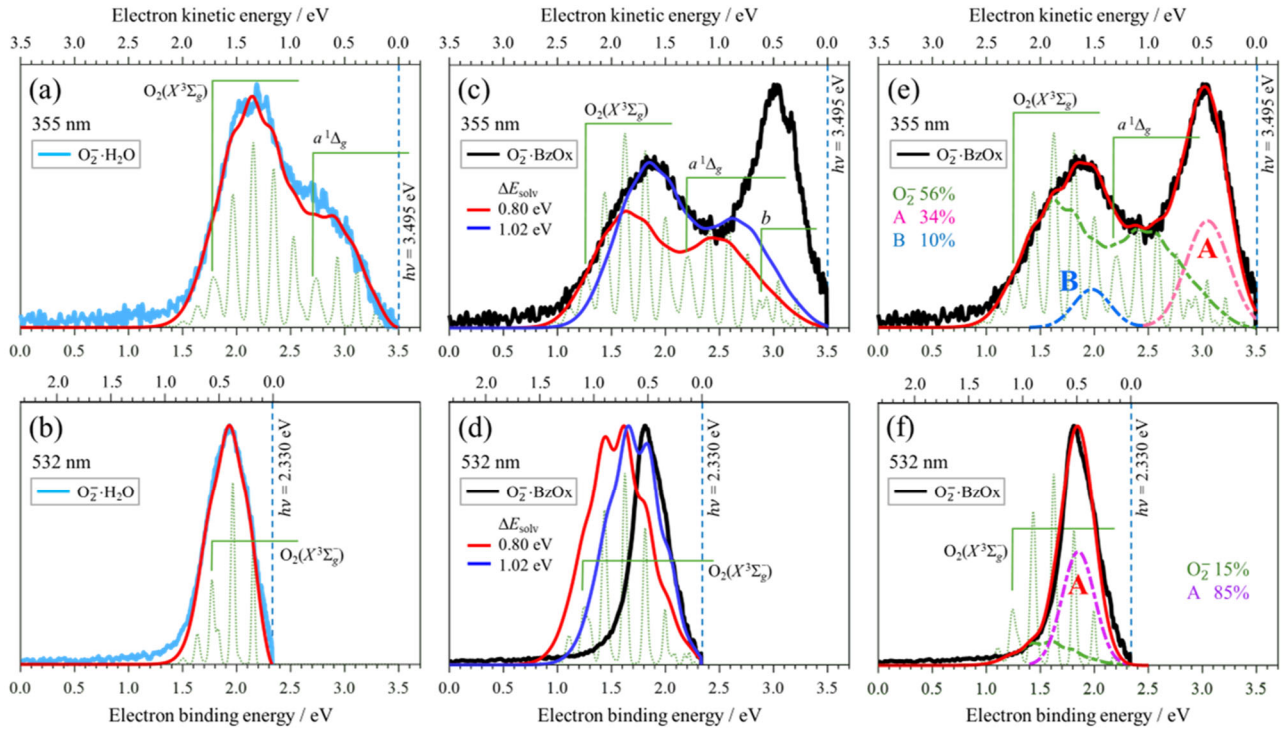

Figure 4. (a)-(b) The 355 and 532 nm O_2^-·H_2O photoelectron spectra (light blue) reproduced from Figure 3 and their simulations using the direct-photodetachment model (red) with ΔE_{solv} = 1.33 eV. The green dotted traces represent the simulated O_2^- spectra, also shifted by 1.33 eV. (c)-(d) The 355 and 532 nm O_2^-·BzOx photoelectron spectra (black) reproduced from Figure 3 and their simulations using the direct-photodetachment model with ΔE_{solv} = 0.80 eV (red) and 1.02 eV (deep blue). The green dotted traces are the O_2^- spectra shifted by 0.80 eV. (e)-(f) The 355 and 532 nm O_2^-·BzOx photoelectron spectra (black) reproduced from Figure 3 and their global simulations (red) using a combination of direct-photodetachment transitions with ΔE_{solv} = 0.80 eV (dash-dotted green) and autodetachment bands A and B corresponding to charge transfer to the temporary cluster states $O_2(a\,^1\Delta_g)$·$BzOx^-$(A) and $O_2(^3\Sigma_g^-)$·$BzOx^-$(B) in (e) and $O_2(X^3\Sigma_g^-)$·$BzOx^-$(A) in (f). The A and B bands are scaled by 1/2 relative to the direct-detachment spectra for clarity. The green dotted traces represent the simulated O_2^- spectra shifted by 0.80 eV.

Figure 5

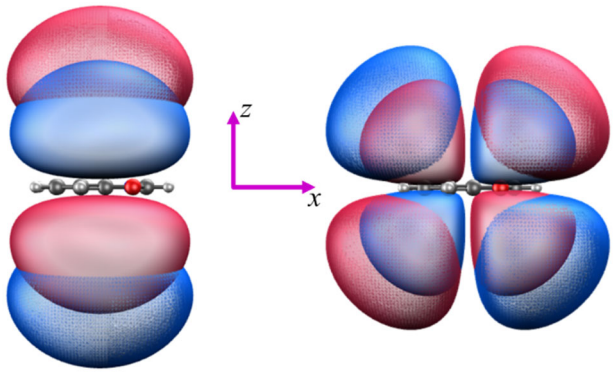

Figure 5. The least diffuse and most diffuse among the added p_z (left) and d_{xz} (right) basis functions, plotted with an isosurface value of 0.008 a.u.

Figure 6

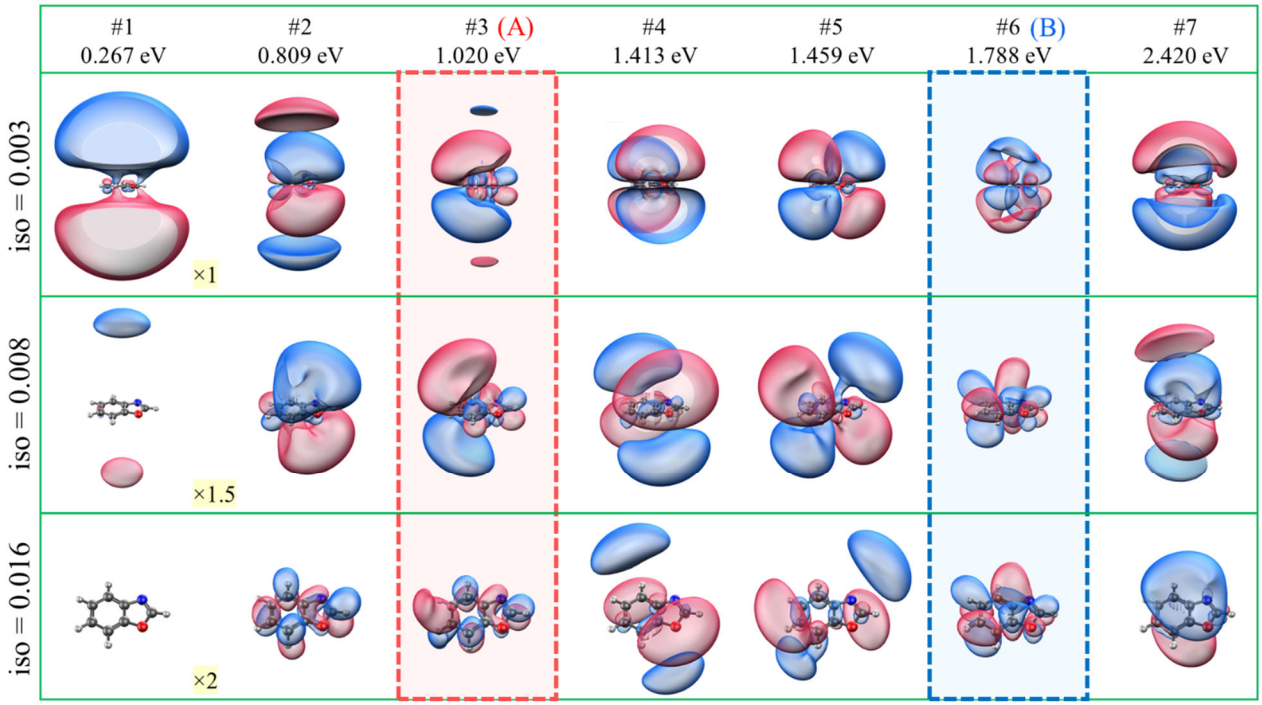

Figure 6. The (left) Dyson orbitals for the lowest seven CAP-free electron attachment solutions for an isolated neutral benzoxazole molecule. Each orbital is shown using three different isosurface values, orientations, and zoom levels, as explained in the text. The solutions within the red (#3) and blue (#6) shaded frames give rise to CAP-stabilized anionic resonances A and B, respectively.

Figure 7

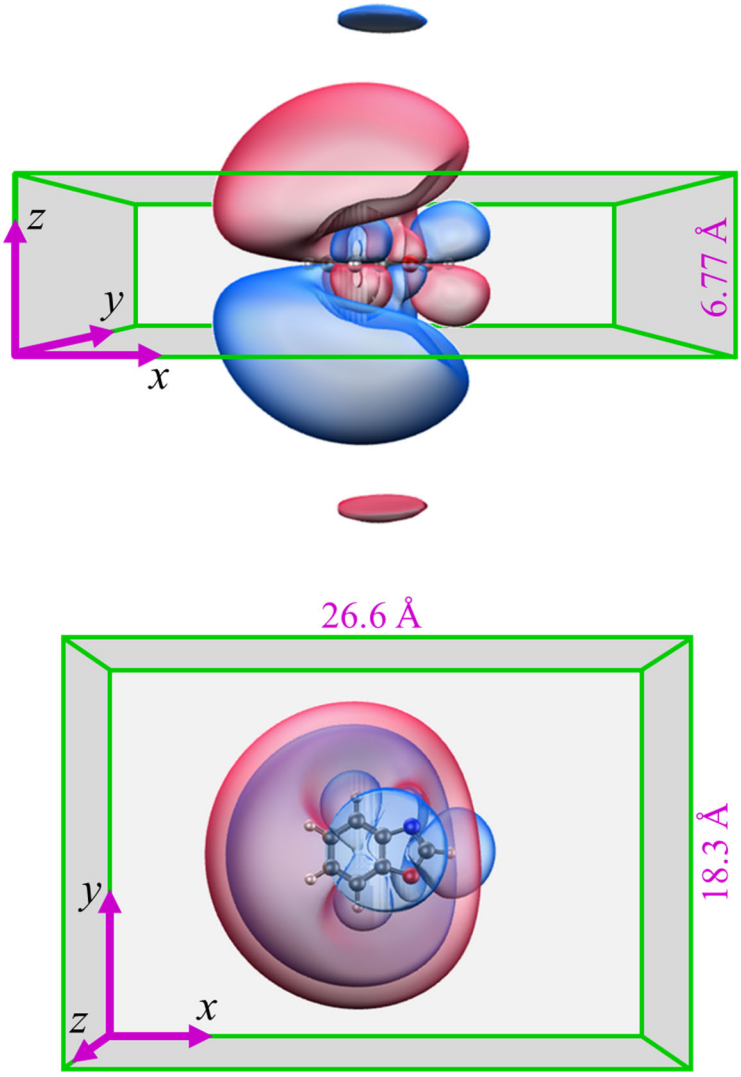

Figure 7. The box representing the CAP onset boundary in the CAP-EOM-EA-CCSD calculations, with the dimensions given in Angstroms. Two different projections are shown, along with one of the CAP-free Dyson orbitals from Figure 6 (root #3, iso = 0.003).

Figure 8

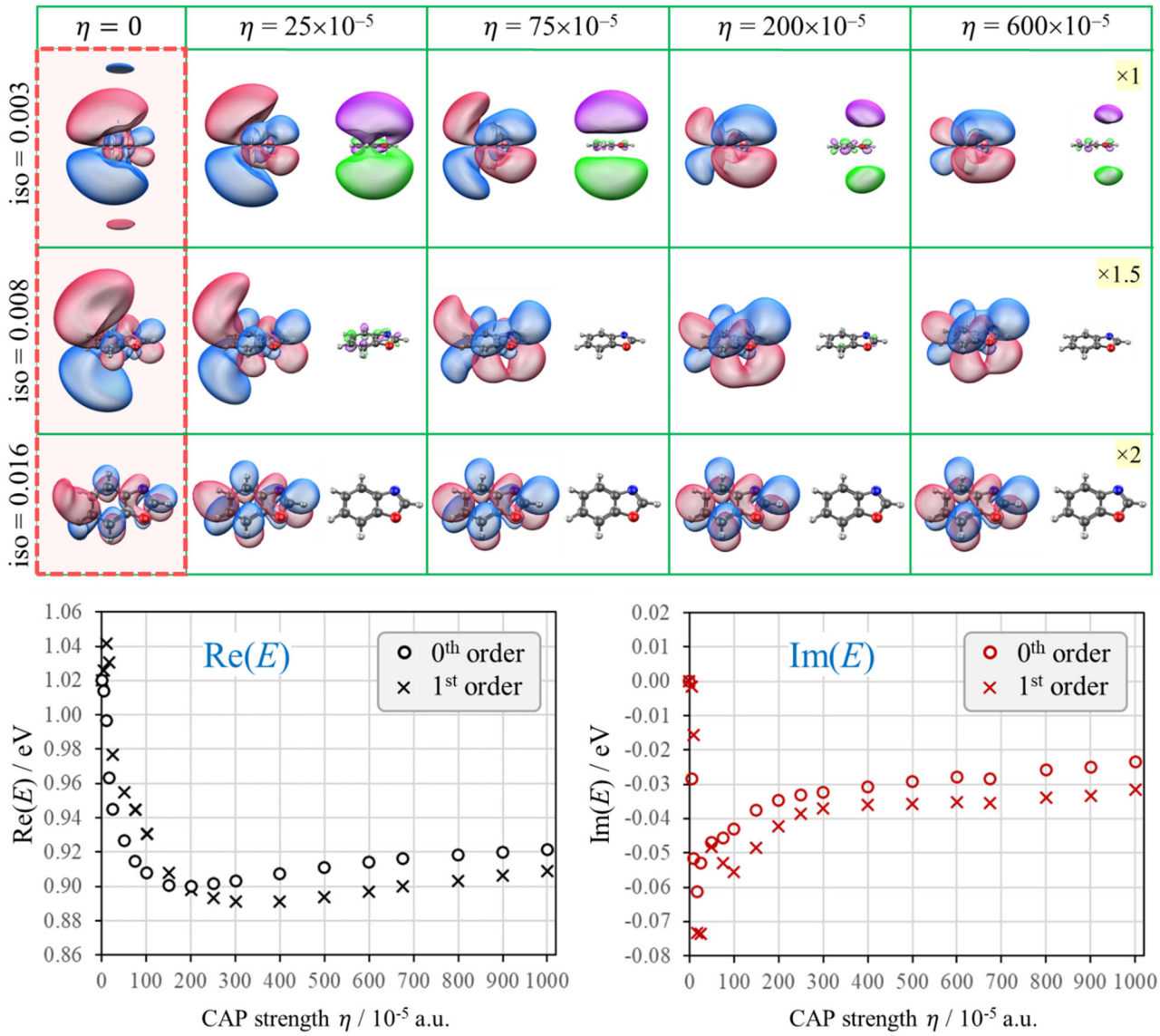

Figure 8. The CAP-induced evolution of anionic resonance A in benzoxazole. The top part shows the (c-normalized left) Dyson orbital originating from root 3 (A) in Figure 6 for several selected CAP strengths (η). Similar to Figure 6, the orbitals are shown using three different iso values, orientations, and zoom levels, as explained in the text. The real parts of the orbitals are shown using red and blue, while their imaginary components are plotted in purple and green. The bottom part of the figure shows the changes in the real and imaginary parts of the energy eigenvalues (0^{th} and 1^{st} order) with increasing η.

Figure 9

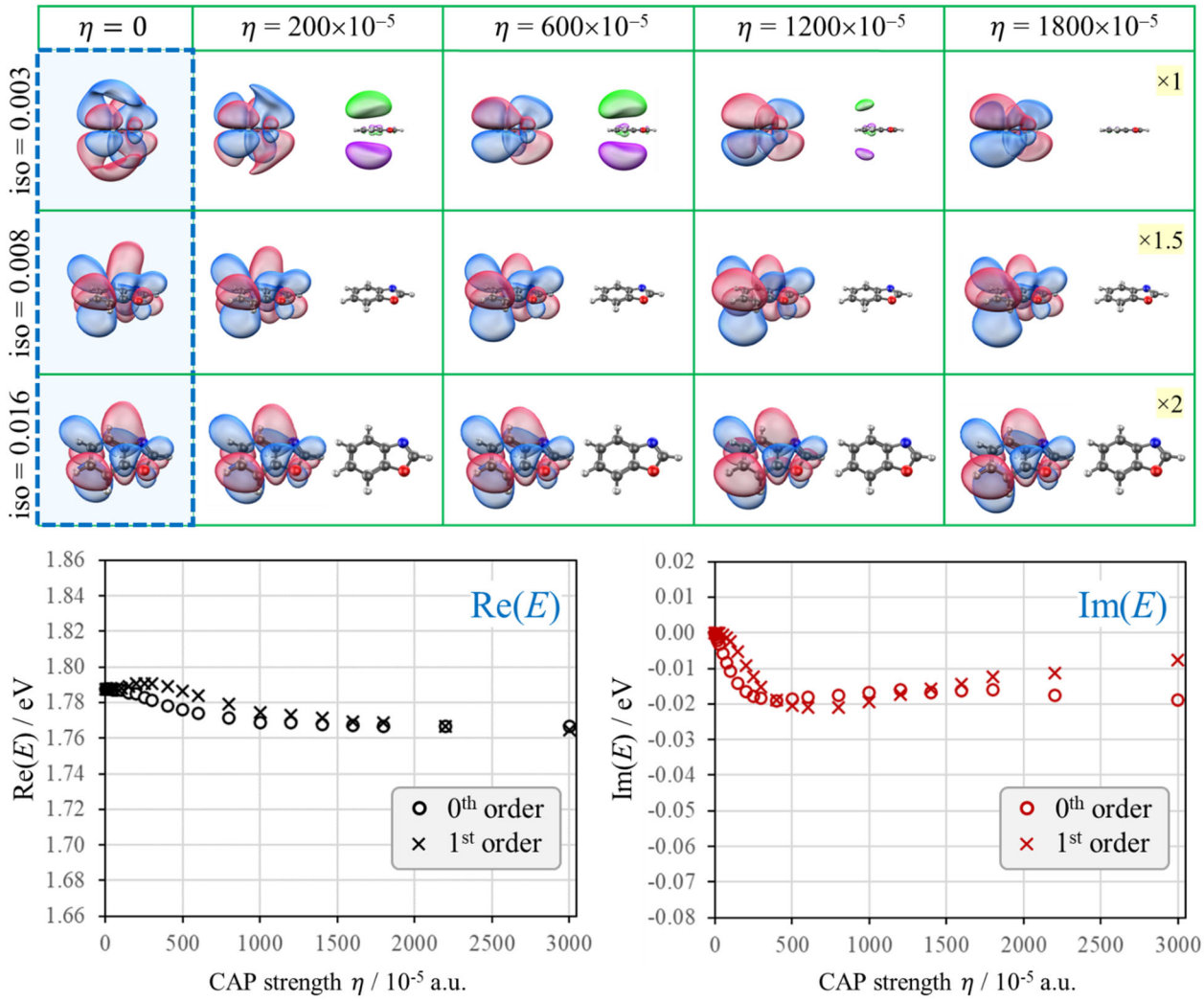

Figure 9. The CAP-induced evolution of anionic resonance B in benzoxazole. The top part shows the (c-normalized left) Dyson orbital originating from root 6 (B) in Figure 6 for several selected CAP strengths (η). Similar to Figure 6, the orbitals are shown using three different iso values, orientations, and zoom levels, as explained in the text. The real parts of the orbitals are shown using red and blue, while their imaginary components are plotted in purple and green. The bottom part of the figure shows the changes in the real and imaginary parts of the energy eigenvalues (0^{th} and 1^{st} order) with increasing η.

Figure 10

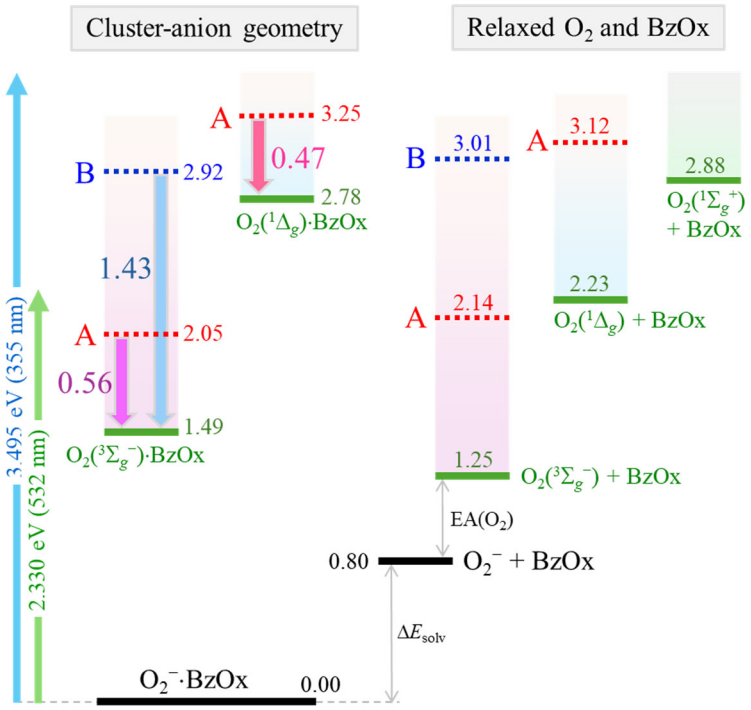

Figure 10. Summary of the O_2^-·BzOx cluster and relaxed fragment energetics. All energies are indicated in eV relative to the optimized O_2^-·BzOx cluster structure. The left half of the diagram is based on the calculations for the O_2^-·BzOx structure. Solid green lines correspond to the $O_2(^3\Sigma_g^-)$·BzOx and $O_2(^1\Delta_g)$·BzOx neutral-state energies at the O_2^-·BzOx geometry. The red and blue dotted lines represent the A and B $BzOx^-$ resonances embedded in the $O_2(^3\Sigma_g^-)$·BzOx + e^- and $O_2(^1\Delta_g)$·BzOx + e^- continua. The right side of the figure represents similar states for the non-interacting and relaxed O_2 and BzOx molecules. A summary of all energy determinations is given in Table S1 in Supporting Information.

Figure 11

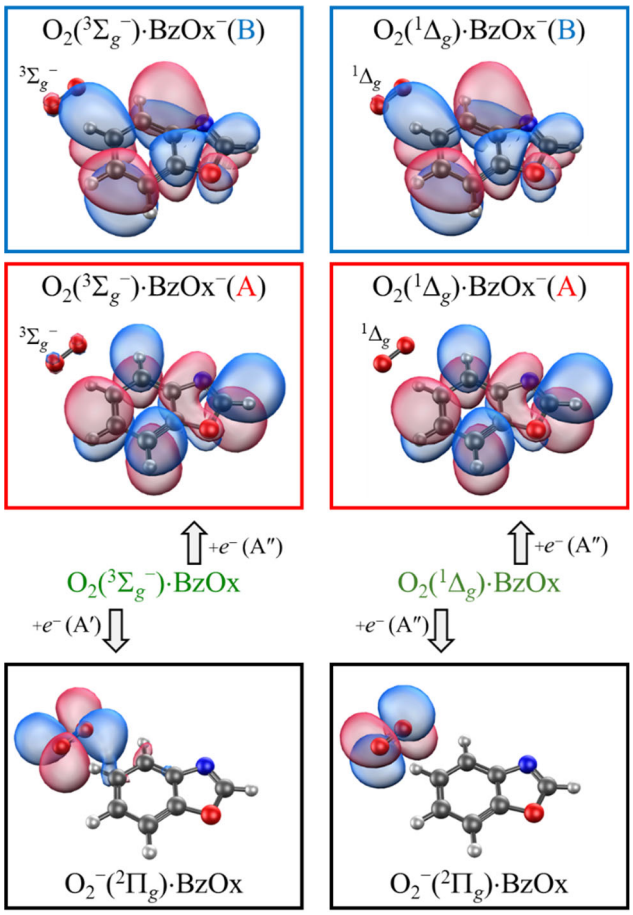

Figure 11. The Dyson orbitals for six different electron-attachment transitions in the O_2·BzOx cluster at the O_2^-·BzOx cluster-anion geometry. The left and right sides correspond to electron attachment to the $O_2(^3\Sigma_g^-)$·BzOx (triplet) and $O_2(^1\Delta_g)$·BzOx (singlet) reference, respectively. The lowest-energy EOM-EA-CCSD solutions for each reference yield the ground cluster-anion state with the excess electron localized on the O_2^- moiety. The higher-energy CAP-EOM-EA-CCSD solutions yield the charge-transfer states, with the electron localized on the $BzOx^-$ moiety (resonance A or B) and the neutral O_2 molecule remaining in its reference state. All orbitals are shown with iso values of 0.016 a.u.

TOC Graphic

(3.25 in × 1.75 in)